ANNUAL REVIEWS

Mass Transfer at the Ocean–Atmosphere Interface: The Role of Wave Breaking, Droplets, and Bubbles

Luc Deike

Department of Mechanical and Aerospace Engineering and High Meadows Environmental Institute, Princeton University, Princeton, New Jersey, USA; email: ldeike@princeton.edu

ANNUAL REVIEWS CONNECT

www.annualreviews.org

- Download figures
- Navigate cited references
- Keyword search
- Explore related articles
- Share via email or social media

Keywords

air–sea interaction, wave breaking, bubbles, gas transfer, sea spray, turbulence

Abstract

Breaking waves modulate the transfer of energy, momentum, and mass between the ocean and atmosphere, controlling processes critical to the climate system, from gas exchange of carbon dioxide and oxygen to the generation of sea spray aerosols that can be transported in the atmosphere and serve as cloud condensation nuclei. The smallest components, i.e., drops and bubbles generated by breaking waves, play an outsize role. This fascinating problem is characterized by a wide range of length scales, from wind forcing the wave field at scales of $\mathcal{O}(1$ km–0.1 m$)$ to the dynamics of wave breaking at $\mathcal{O}(10$–0.1 m$)$; air bubble entrainment, dynamics, and dissolution in the water column at $\mathcal{O}(1$ m–10 μm$)$; and bubbles bursting at $\mathcal{O}(10$ mm–1 μm$)$, generating sea spray droplets at $\mathcal{O}(0.5$ mm–0.5 μm$)$ that are ejected into atmospheric turbulent boundary layers. I discuss recent progress to bridge these length scales, identifying the controlling processes and proposing a path toward mechanistic parameterizations of air–sea mass exchange that naturally accounts for sea state effects.

1. INTRODUCTION

Sea spray generation function: the size-dependent number of droplets generated per unit area of ocean surface, per unit time

$\Lambda(c)$: the breaking distribution, with $\Lambda(c) \, dc$ the average length of breaking crests moving at a speed between c and $c + dc$, which characterizes the breaking statistics

Physical processes at the ocean–atmosphere interface have a large effect on climate and weather by controlling the transfer of momentum, energy, and mass. Without wave breaking, transport between the ocean and the atmosphere occurs through slow conduction and molecular diffusion, while wave breaking is a transitional process from laminar to turbulent flow. When waves are breaking, the surface experiences dramatic changes, with sea spray ejection in the atmosphere and air entrainment into the ocean water. The dynamics and statistics of wave breaking in a particular ocean location depend mainly on the local wave state and not on the wind velocity, while current parameterizations for air–sea interactions in oceanic and atmospheric models remain based exclusively on wind speed.

The processes associated with breaking waves at the ocean surface span multiple fields of oceanic and atmospheric sciences, as breaking waves regulate the ocean–atmosphere interaction from local to global scales. Breaking limits the height of ocean waves, transfers momentum from waves to currents, and modulates upper-ocean turbulence (Melville 1996, Sullivan & McWilliams 2010, Cavaleri et al. 2012, Perlin et al. 2013). In the present review, I focus on the role of wave breaking, and the associated bubbles entrained in water and drops ejected in the atmosphere, in controlling mass exchange. Air bubbles entrained by breaking contribute to gas exchange, with approximately 30% of the CO_2 released into the atmosphere taken up by the ocean. Recent reviews by Wanninkhof et al. (2009), Garbe et al. (2014), and Woolf et al. (2019) have discussed air–sea gas exchange and highlighted the remaining uncertainties in quantifying the role of air bubbles entrained by wave breaking in the transfer of gases critical to the climate system such as O_2 and CO_2. Breaking is responsible for the formation of sea spray through direct atomization, and while small bubbles may be dissolved into the water column, larger bubbles entrained by breaking rise back to the surface and collapse. This generates spray that is transported into the atmosphere and ultimately evaporates, leaving water vapor, which is important for the thermodynamics of the atmosphere, and salt crystals, which affect the radiative balance of the atmosphere and form cloud condensation nuclei, as reviewed by Lewis & Schwartz (2004), de Leeuw et al. (2011), and Veron (2015). The implications of organic and sea salt aerosols on atmospheric chemistry have been reviewed by Quinn et al. (2015), Cochran et al. (2017), and Bertram et al. (2018) and highlight the importance of understanding the processes producing sea spray droplets.

These studies highlight the uncertainties in bubble-mediated gas exchange and the production of sea spray, which are represented in large-scale models by the gas transfer velocity and the sea spray generation function. These parameters control the associated fluxes of gases, moisture, and sea salt, which are key to the climate system and are usually only parameterized as a function of wind speed, while local processes are more tightly controlled by the sea state.

The uncertainties in studying both bubble-mediated gas transfer and the production of sea spray aerosols by bubble bursting come from the large range of length scales involved, summarized in **Figure 1**, which range from bubbles at $\mathcal{O}(1 \, \mu m – 10 \, mm)$ to breaking waves at $\mathcal{O}(0.1–10 \, m)$, large-scale wave patterns at $\mathcal{O}(10 \, m – 1 \, km)$, and wind forcings; from the difficulty in conducting field measurements (especially at high wind speed); and from the lack of connections between idealized mechanistic descriptions of individual processes and ocean conditions. Above a certain wind speed, typically 7 m/s, waves start to break, entraining air bubbles that are visible in whitecaps at the ocean surface. The breaking fronts of length distribution $\Lambda(c)$ moving at a certain speed c are illustrated in **Figure 1a**, following the representation introduced by Phillips (1985), which we use to relate the breaking distribution to the air–sea fluxes associated with the entrained bubbles. The speed of the breaking fronts in the field typically ranges from 1 to 10 m/s. A single breaking event is illustrated in **Figure 1b**, characterized by its height at breaking h, $\mathcal{O}(0.1–10 \, m)$, which, together
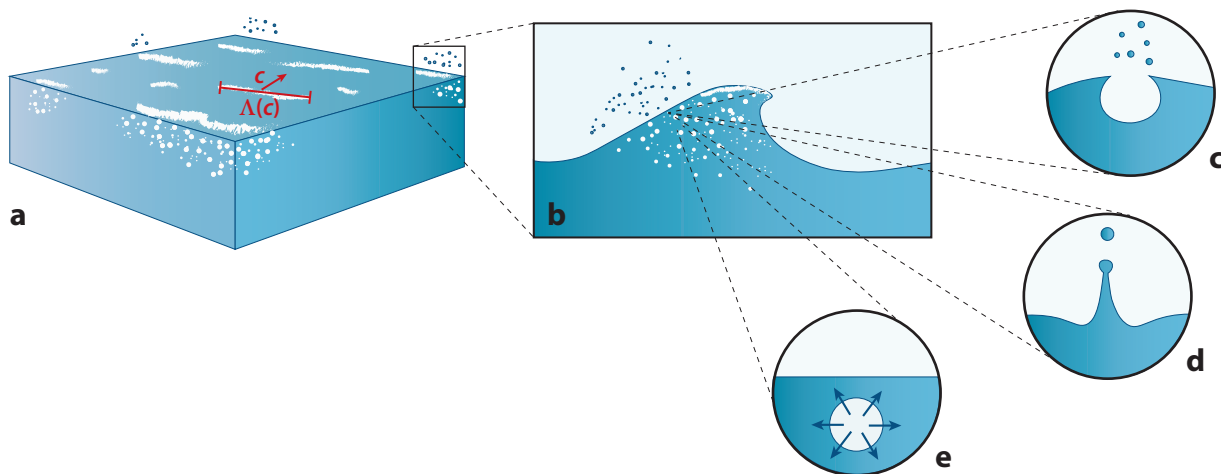
Figure 1

The multiscale approach discussed in this review to model mass exchange due to breaking waves, drops, and bubbles. At moderate to high wind speeds, breaking waves form whitecaps on the ocean surface. (*a*) The breaking statistics can be described by the length distribution $\Lambda(c)$ of breaking crests moving at speed c, typically from 1 to 10 m/s. (*b*) Each breaker's dynamics is assumed to be self-similar and is described by its speed c and slope S, leading to scaling models for the associated energy dissipation, air entrainment, and bubble statistics. At the smallest scales, bubbles with sizes R_b ranging from $\mathcal{O}(1\ \mu m)$ to $\mathcal{O}(10\ mm)$ (*c,d*) burst at the surface to produce liquid sea sprays via (*c*) film and (*d*) jet drops, with sizes r_d ranging from $\mathcal{O}(0.1\ \mu m)$ to $\mathcal{O}(1\ mm)$, and (*e*) exchange gas in the turbulent upper ocean.

with c, controls turbulence generation and bubble plume entrainment. The bubbles entrained by breaking, $\mathcal{O}(1\ \mu m$–$10\ mm)$, evolve in the upper-ocean turbulent flow, exchange gas, and may rise to the surface, where they burst and produce jet and film drops (**Figure 1***c–e*).

Bridging the scales involved in mass exchange between the ocean and the atmosphere has been a longstanding issue, as the associated uncertainties in the production processes propagate into uncertainties in large-scale modeling; thus, such bridging of scales is the focus of this review. Section 2 presents the dynamics of wave breaking, focusing on the properties of the postbreaking two-phase turbulent flow, based on canonical experiments and simulations. Section 3 presents the ocean wave scales, focusing on statistical representations of waves and wave breaking. This is combined with our understanding of the breaking dynamics to obtain a multiscale description of energy dissipation and air entrainment by breaking waves, which can then be used to estimate mass fluxes controlled by breaking waves at the ocean–atmosphere interface. I describe two important applications of this framework: gas exchange (Section 4) and the production of sea spray by bursting bubbles (Section 5), yielding sea state formulations for the gas transfer velocity and sea spray generation function.

The scope of this review is broad, and each of these processes deserves its own review. I offer sincere apologies to those whose work on mass exchange at the air–sea interface I have overlooked, whether as a result of editorial constraints or by my own omission. I focus on providing a consistent framework to bridge the scales, presenting scaling models derived from mechanistic studies at the scales of bubbles, droplets, and breaking waves combined with a statistical representation of the sea state. I show how this strategy can provide sea state–dependent formulations for ocean–atmosphere fluxes, focusing on bubble-mediated gas transfer and the production of sea spray by bursting bubbles.

Jet drops: drops ejected when a jet forms from a bubble cavity collapse

Film drops: drops ejected during the bursting of bubbles' thin cap films

2. WAVE BREAKING DYNAMICS: ENERGETICS AND AIR BUBBLE ENTRAINMENT

2.1. Energy Dissipation by a Breaking Wave and the Scales of Breaking

I start by presenting the fundamental understanding of energy dissipation by breaking waves and the controlling physical parameters, the breaking speed and wave slope.

2.1.1. Canonical breaking waves in the laboratory and in direct numerical simulations.
The importance and complexity of deep ocean breaking waves, combined with the difficulties in measuring and observing a two-phase turbulent process at sea, have driven experimental, numerical, and theoretical work that aims to elucidate the physics of breaking waves.

Numerous studies have investigated the routes leading to breaking, including linear and nonlinear focusing, as well as modulation instability. The quest for a universal breaking criterion remains an outstanding challenge, while the definition of a breaking event is itself nontrivial due to the issues of early interface disturbance, microbreaking, parasitic capillaries, and air entrainment (Melville 1982, Rapp & Melville 1990, Duncan 2001, Banner & Peirson 2007, Perlin et al. 2013, Saket et al. 2017).

Here, I focus on postbreaking properties and characterize the transition from a laminar wave flow to a two-phase turbulent flow (Duncan 1981, Rapp & Melville 1990, Lamarre & Melville 1991). Laboratory experiments using the linear focusing method have allowed researchers to generate highly reproducible breaking packets, illustrated in **Figure 2**, which, combined with progress
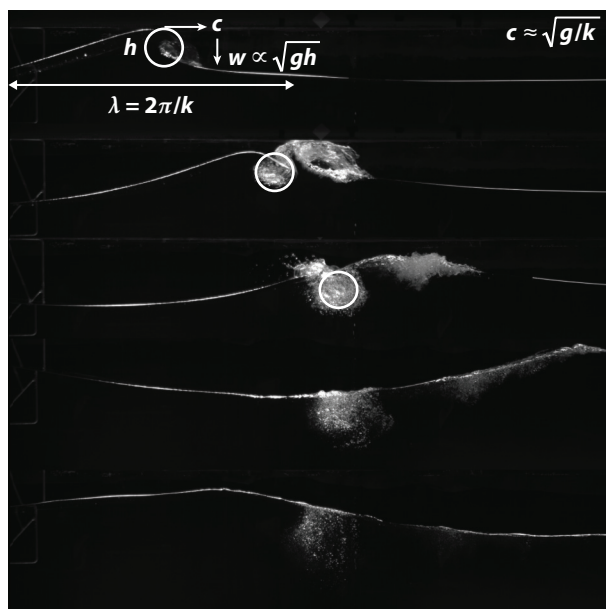

Figure 2

A breaking sequence in the laboratory indicating the breaking scales; the breaker crest speed c, height h, and wavelength λ; the jet ballistic velocity $w \sim \sqrt{gh}$; and the resulting bubbly turbulent cloud, with a lifetime τ_b. The sequence shows steepening and jet formation, impact at speed w, the creation of a turbulent bubbly cloud of cross section $A \propto h^2$, and plume evolution with the breakup of bubbles, which rise back to the surface and burst.

in two-phase flow measurement techniques, have led to high-quality data of energy dissipation, turbulence, and current generation (Rapp & Melville 1990, Melville 1994, Melville et al. 2002, Banner & Peirson 2007, Drazen et al. 2008, Tian et al. 2010). The main controlling variables of the postbreaking flow have been identified as the breaker speed c and wave slope $S = hk$, where h is the breaking height and k is the characteristic wavenumber.

Separately, numerical simulations have brought insights into the breaking dynamics, starting with nonlinear free surface potential solvers resolving up to the breaking point (Dommermuth et al. 1988, Longuet-Higgins & Dommermuth 1997), as well as insights into spilling breakers and microbreakers or parasitic capillary waves (Tsai & Hung 2007, Melville & Fedorov 2015). More recently, direct numerical simulations (DNS) of the two-phase Navier–Stokes equations have started to become available to capture postbreaking properties, both in two dimensions (Chen et al. 1999, Iafrati 2009, Deike et al. 2015) and finally in three dimensions (Deike et al. 2016, Wang et al. 2016, Yang et al. 2018, Chan et al. 2020, Mostert et al. 2021). These DNS usually consider compact wave trains at moderate Reynolds number and have demonstrated their ability to reproduce energy dissipation and other postbreaking features from laboratory experiments to explore the resulting two-phase turbulent flow. Together with DNS, large eddy simulations (LES) help to fill the gap between the DNS and the laboratory scales (Lubin & Glockner 2015, Derakhti & Kirby 2016).

2.1.2. The inertial scaling for energy dissipation by breaking waves.

Duncan (1981) and Phillips (1985) have described the dissipation rate due to breaking, per unit length of breaking crest ϵ_l, assuming that the breaking zone extends down the forward face of the wave over a fixed fraction of its amplitude and that its shape is geometrically similar for waves of different scales, so that

$$\epsilon_l = b\rho c^5/g, \qquad\qquad 1.$$

where g is gravity and ρ is the water density. This introduces the nondimensional breaking parameter b, first assumed to be a nondimensional constant but subsequently shown by extensive experimental scrutiny to vary over several orders of magnitude when varying the breaking wave slope $S = hk$ (Duncan 1981, Rapp & Melville 1990, Drazen et al. 2008, Tian et al. 2010).

Drazen et al. (2008) proposed that the breaking strength and resulting turbulence are controlled by the local breaking height together with the breaker speed. The total dissipation rate per unit breaking crest length ϵ_l can be related to the local turbulent dissipation rate ε considering that the turbulence is confined to a volume $\mathcal{V} = AL_c$ of cross section $A \simeq \pi h^2/4$ (Drazen et al. 2008) and breaking crest length L_c, so that $\epsilon_l = \rho A \varepsilon$. The local turbulent dissipation rate after impact is described by a turbulent inertial scaling and is linked to the integral length scale, $\sim h$, and breaking intensity quantified by the ballistic velocity of the falling jet, $w \sim \sqrt{gh}$ (Drazen et al. 2008, Erinin et al. 2019). The local turbulence dissipation rate then reads

$$\varepsilon \propto \sqrt{gh}^{\,3}/h, \qquad\qquad 2.$$

so that the dissipation rate per unit length of breaking crest is $\epsilon_l = \rho A \varepsilon = \chi S^{5/2} \rho c^5/g$, with χ an $\mathcal{O}(1)$ constant; the breaking parameter $b = \chi S^{5/2}$ is now a function of the breaking slope. This local scaling has been extensively tested and related to the initial conditions of the breaking packet (slope, bandwidth, and speed) using laboratory experiments (Duncan 1981, Rapp & Melville 1990, Banner & Peirson 2007, Drazen et al. 2008, Grare et al. 2013) and numerical simulations (Iafrati 2009; Deike et al. 2015, 2016; Derakhti & Kirby 2016; De Vita et al. 2018). **Figure 3a** shows
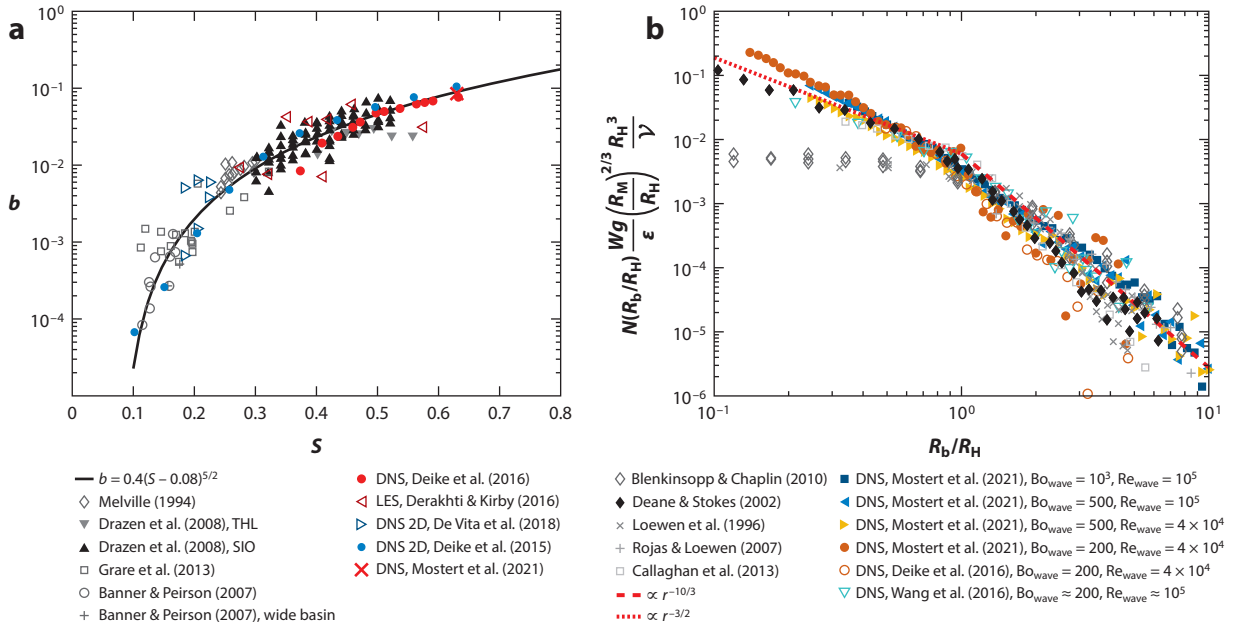
b: the breaking parameter is a nondimensional measure of the energy dissipation and is mainly a function of breaker speed and slope

Figure 3

Energy dissipation and bubble size distributions from laboratory experiments and numerical simulations of canonical breaking waves. Black and gray symbols are experimental data, while colored symbols are from numerical work. (*a*) Breaking parameter b as a function of the initial wave slope S, for DNS, LES, and laboratory experiments. The solid line is the semiempirical formulation based on the inertial argument, $b = 0.4(S - 0.08)^{5/2}$ (Equation 3; Romero et al. 2012). All data are very well captured by the solid line given the complexity of the process and the differences in initiating breaking. (*b*) Bubble size distributions as a function of R_b/R_H, where R_b is the bubble radius and R_H is the Hinze scale, over the active breaking time, normalized following Equation 6 for the data from Deike et al. (2016) and Mostert et al. (2021) and for the experimental data from Deane & Stokes (2002) (other data are arbitrarily scaled vertically since not enough information is provided). The data collapse onto a single curve $R_b^{-10/3}$ for the super-Hinze regime, and most data collapse onto $R_b^{-3/2}$ for the sub-Hinze regime. SIO and THL design data from Drazen et al. (2008). Abbreviations: DNS, direct numerical simulations; LES, large eddy simulations; SIO, Scripps Institution of Oceanography wave tank; THL, Tainan Hydraulics Laboratory wave tank.

b as a function of the slope S, with the data very well described by the semiempirical scaling that accounts for a breaking threshold defined by a critical slope S_0 (Romero et al. 2012),

$$b = \chi_T(S - S_0)^{5/2},\qquad\qquad 3.$$

where $\chi_T = 0.4$ and $S_0 = 0.08$ are adjusted to the data.

We note that the breaking speed has been observed to move at a velocity c_b slightly below the phase velocity, $0.8c \le c_b \le c$ (Rapp & Melville 1990, Banner & Peirson 2007, Saket et al. 2017). This has motivated discussions on the definition of the slope, either from upstream conditions or closer to the breaking point, which impacts the coefficients χ_T and S_0. This underlines the fact that a critical slope is an imperfect breaking criterion, with variability among various experiments and types of breakers, and it has prompted extensive work on kinematic thresholds (Perlin et al. 2013, Saket et al. 2017, Derakhti et al. 2020).

Nevertheless, this formulation for the breaking parameter and energy dissipation provides constraints on the wave breaking energy budget, and in the following we consider that the breaking speed c and the wavenumber k can be related to the dispersion relation of ocean gravity waves in

deep water, $c = \sqrt{g/k}$. Note that scaling arguments, using the breaking height and speed as the controlling scales, have been proposed to describe the generation of vorticity (Pizzo & Melville 2013), current (Pizzo et al. 2016), and surface drift induced by breaking (Deike et al. 2017b, Pizzo et al. 2019).

2.2. Air Entrainment and Bubble Distribution Under a Breaking Wave

Together with total air entrainment, the bubble size distribution $N(R_b)$ is the most important characteristic of the bubble formation process, as it controls mass exchange. Duncan (1981), Lamarre & Melville (1991), Blenkinsopp & Chaplin (2010), Deike et al. (2016), and Mostert et al. (2021) have shown that the breaker geometry constrains the maximum volume of air entrained and that the air cavity cross section scales as $A \propto b^2$ with entrainment of a relatively homogeneous bubble cloud up to a depth b (see **Figure 2**).

Garrett et al. (2000) proposed a steady model of the bubble size distribution (per unit volume) $N(R_b)$ of a turbulent breakup cascade, with R_b the bubble radius, assuming that the air flow rate per unit volume of water Q is constant, $N(r) \propto Q$, and that the process is controlled only by the local (time-averaged) turbulent dissipation rate ε, so that dimensional analysis yields

$$N(R_b) \propto Q\varepsilon^{-1/3}R_b^{-10/3}. \qquad 4.$$

This result can also be understood by a population-balance argument, with the breakup cascade local in scale and the breakup time driven by the turbulence at the scale of the bubble, $\tau_c \propto \varepsilon^{-1/3}R_b^{2/3}$, which yields $N(R_b) \propto R_b^{-10/3}$. Several experimental studies (Loewen et al. 1996, Deane & Stokes 2002, Rojas & Loewen 2007, Blenkinsopp & Chaplin 2010) have confirmed this scaling, together with recent DNS of breaking waves (Deike et al. 2016, Wang et al. 2016, Chan et al. 2020, Mostert et al. 2021) (**Figure 3**). The turbulent breakup cascade has also been characterized by DNS of single large bubbles or droplets breaking in a homogeneous and isotropic turbulent flow (Soligo et al. 2019, Rivière et al. 2021).

The local turbulent breakup cascade assumes an inertial subrange and a direct cascade process: Air is injected at large scales (large bubbles) by the entrainment process and turbulent fluctuations break them into smaller bubbles. The cascade process ends at the scale where surface tension prevents further bubble breakup, known as the Hinze (1955) scale,

$$R_H = \mathcal{C}(\gamma/\rho)^{3/5}\varepsilon^{-2/5}, \qquad 5.$$

where $\mathcal{C}$ is a dimensionless constant of $\mathcal{O}(1)$ (Martinez-Bazan et al. 1999, Perrard et al. 2021, Rivière et al. 2021). Under typical breaking conditions, the Hinze scale is $R_H \approx 1$–2 mm, and about 95% of the entrained air volume is contained in super-Hinze ($R_b > R_H$) bubbles (Deane & Stokes 2002, Mostert et al. 2021).

Deane & Stokes (2002) have reported the statistics of bubbles below the Hinze scale as $N(R_b) \propto R_b^{-3/2}$, while other experimental measurements have shown a large scatter, as illustrated in **Figure 3**. Recent DNS of breaking waves and bubble breakup have provided further evidence for the $N(R_b) \propto R_b^{-3/2}$ regime (Mostert et al. 2021, Rivière et al. 2021), with production due to entrainment at impact (Chan et al. 2020, Mostert et al. 2021) and the fragmentation of highly deformed, large super-Hinze bubbles, yielding a nonlocal cascade (Rivière et al. 2021).

Deike et al. (2016) and Mostert et al. (2021) have combined the geometrical constraint of the entrained bubble cloud with an energy balance between buoyancy forces and turbulent dissipation and have proposed a relationship describing the time evolution of the air entrained by the bubble plume and the turbulence dissipation rate. Integrating over the breaking time, or bubble plume time τ_b, and considering the entrained cavity size R_M as the injection size so that $AL_c \equiv \mathcal{V} \propto R_M^2L_c$,

$N(R_b)$: the bubble size distribution under a breaking wave is separated into two regimes; for $R_b > R_H$, a turbulent breakup cascade is observed, $N(R_b) \propto R_b^{-10/3}$, and contains ~95% of the initial entrained volume, and for $R_b < R_H$, most data follow $N(R_b) \propto R_b^{-3/2}$

R_H: the Hinze scale compares the action of surface tension and turbulence and corresponds to the critical size below which bubbles do not break under water turbulence

the size distribution reads

$$N(R_b/R_H) = \frac{B}{2\pi} \frac{\varepsilon}{Wg} \left(\frac{R_b}{R_H}\right)^{-10/3} \frac{\mathcal{V}}{R_H^3} \left(\frac{R_M}{R_H}\right)^{-2/3}. \qquad 6.$$

Here, W is a characteristic plume velocity related to the breaking height and plume lifetime, $\tau_b W \propto h$ (Lamarre & Melville 1991; Callaghan et al. 2013; Deike et al. 2016, 2017a), and $B \approx 0.1$ is a nondimensional constant related to the ratio between the total dissipation rate and the contribution to air entrainment. The sub-Hinze regime is obtained by continuity. As shown in **Figure 3b**, this model describes very well the experimental and numerical data available (with some scatter remaining in the sub-Hinze regime). The total volume of entrained air during the breaking process is obtained by integration, assuming separation of scales $R_H \ll R_M$:

$$V = \int_{R_H}^{R_M} (4\pi/R_b)R_b^3 N(R_b)\,dR_b = Bb\frac{L_c c^5}{W g^2}. \qquad 7.$$

Equation 7 provides a constraint on air entrainment based on the characteristic scales of breaking waves, namely, their speed c and slope S (since $b \propto S^{5/2}$).

3. OCEAN WAVES: WAVE BREAKING STATISTICS AND DYNAMICS

We have discussed canonical breaking waves in well-controlled laboratory and numerical experiments and introduced scaling laws for the energy dissipation and air bubble entrainment in the near-surface turbulent layer. While uncertainties remain, these relationships serve as a basis to construct mechanistic models of air–sea fluxes by assuming that breaking waves in the field behave similarly and can be described by their local breaking crest speed and slope. We now characterize the statistics of waves and breaking waves as a function of large-scale wind forcing.

3.1. The Wave Spectrum

The sea state can be represented by the wave surface elevation $\eta(x, y)$, which depends on wind, currents, and the history of the spatially evolving wave field. The wave field is composed of a large range of wave scales, from gravity–capillary waves with wavelengths on the order of centimeters to swells of wavelength $\mathcal{O}(100\ \text{m})$, and is treated in the Fourier space via the wave spectrum.

3.1.1. Source terms. The directional wave spectrum at the ocean surface $F(\mathbf{k})$ describes the wave energy density per wavenumber scale with $\langle \eta^2 \rangle = \int F(\mathbf{k})\,d\mathbf{k}$, the variance of the wave surface elevation. Here we briefly summarize some essential results to model the wave spectrum, relating the time evolution of the spectrum to source terms [see the book by Komen et al. (1996) for an extensive review]. Locally the wave field is related to the action of the wind as it inputs energy and momentum into the waves, leading to wave growth, nonlinear transfer through the scales (both forward and inverse cascades are possible for surface gravity waves), and dissipation (mainly by breaking waves). All of these processes are in principle dynamically coupled. However, within a statistical description, the spectral evolution of the wave spectrum is obtained by solving the wave action equation, which relates the Lagrangian derivative of the spectral density of a wave packet at its group speed in both physical and spectral spaces to source terms that can input, output, and transfer energy through the scales (Komen et al. 1996, Ardhuin et al. 2010):

$$\frac{dN(\mathbf{k})}{dt} = (S_{\text{wind}} + S_{\text{diss}} + S_{\text{nl}})/\omega, \qquad 8.$$

where $N(\mathbf{k}) = F(\mathbf{k})/\omega$ is the wave action and $\omega = \sqrt{gk}$ is the angular frequency of gravity waves in deep water. The wind forcing depends on the wind friction velocity u_* (defined by the wind stress

at the ocean surface), with a typical functional form $S_{wind} \propto \frac{\rho_a}{\rho_w}(\frac{u_*}{c})^2 \omega F(\mathbf{k})$; there are also empirical formulations for the misalignment between waves and the wind (Miles 1957, Plant 1982, Komen et al. 1996). The nonlinear interaction term S_{nl} transfers energy through the scales through a four-wave resonant process (Hasselmann 1962), while dissipation is mainly due to breaking waves (Phillips 1985).

3.1.2. Equilibrium and saturation ranges. For simplicity, we consider the omnidirectional (angle-integrated) wave spectrum, $\phi(k) = \int F(k, \theta)k\,d\theta$, in order to discuss the spectrum shape. From the peak of the wave spectrum k_p to a transition wavenumber k_n, the spectrum can be described as a balance between the three main source terms, which yields an equilibrium range (Toba 1972, Phillips 1985):

$$\phi(k) = \beta u_* g^{-1/2} k^{-5/2}, \text{ for } k_p < k < k_n. \qquad 9.$$

The Toba constant β is determined empirically and has been described as a function of the wave age, $\beta \approx 0.016(c_p/u_*)^{0.53}$ (Romero & Melville 2010). The corresponding frequency spectrum is $\phi(\omega) = \beta u_* g \omega^{-4}$ given $\phi(k)\,dk = \phi(\omega)\,d\omega$. Note that the peak of the wave spectrum can be related to wind forcing and fetch (the distance over which wind has been blowing without obstruction) through the so-called fetch-limited relationships (Toba 1972, Hasselmann et al. 1973, Romero & Melville 2010).

The equilibrium range is compatible with the independent description of weak-wave turbulence theory, which provides stationary solutions, assuming that energy injection and dissipation occur at very different scales and that there is a nonlinear interaction to transfer energy from large to small scales, yielding a direct cascade, $\phi(k) \propto P^{1/3}g^{-1/2}k^{-5/2}$, where P is a conserved wave energy flux (Zakharov et al. 2012). This result is dimensionally consistent with Equation 9, since $u_* \propto P^{1/3}$. In the weak turbulence framework, an inverse cascade describes the frequency downshift due to wind forcing during the development of the wave spectrum from a calm sea to a fully developed spectrum and yields formulations of the fetch-limited relationships (Zakharov et al. 2015).

At higher frequency, above a transition wavenumber k_n, Phillips (1985) has described the saturation spectrum, where breaking dominates the dynamics, as $k_n \approx (2\hat{B}/\beta)^2 g u_*^{-2}$, with $\hat{B}$ the saturation, which presents a wave age dependency (Romero & Melville 2010, Lenain & Melville 2017b, Lenain & Pizzo 2020). The saturation spectrum follows

$$\phi(k) = \hat{B} k^{-3}, \text{ for } k > k_n. \qquad 10.$$

This description of the wave spectrum has been recently well documented and validated through spatial and temporal field measurements of the wave spectrum (Romero & Melville 2010, Lenain & Melville 2017b, Lenain & Pizzo 2020), as illustrated in **Figure 4a**.

3.2. Breaking Waves in the Open Ocean

Having described the sea state through the wave spectrum, we now need a representation of the wave breaking distribution and the associated air entrainment that directly control the bubble-mediated mass fluxes.

3.2.1. Whitecap coverage. Wave breaking at the ocean surface and the associated air entrainment lead to the presence of whitecaps at moderate to high wind speeds. The whitecap coverage, W_{CC}, is commonly defined as the white patches of bubbles formed at the ocean surface after breaking (Monahan & Muircheartaigh 1980). Despite its apparent simplicity (one only needs a camera to measure white patches at the surface of the ocean!), measurement of whitecap coverage
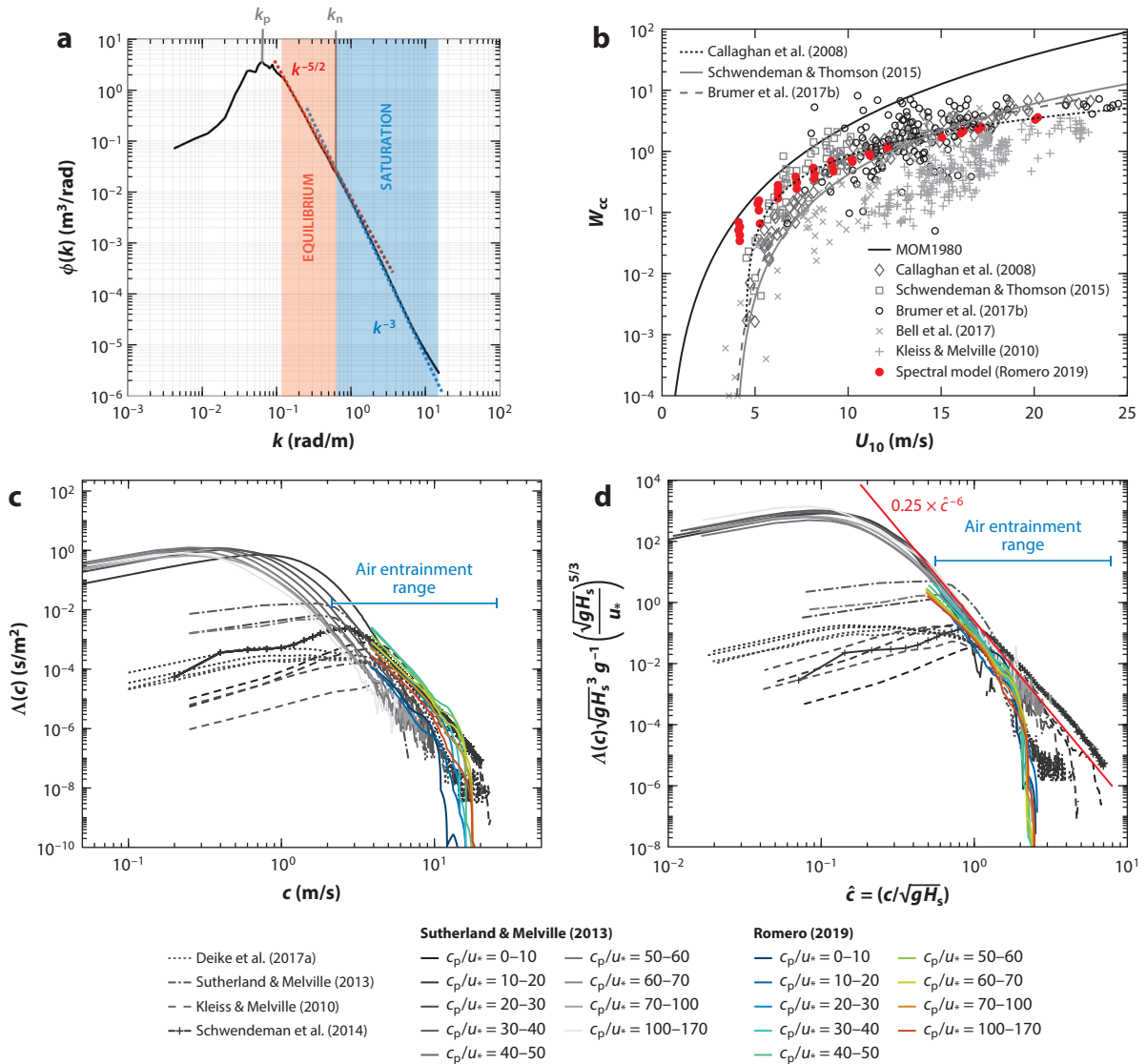
Figure 4

Measurements and spectral modeling of the wave and wave breaking statistics. (*a*) Example of the omnidirectional wave spectrum $\phi(k)$, measured for aircraft using LIDAR (light detection and ranging) (Lenain & Melville 2017b, Lenain & Pizzo 2020), illustrating the equilibrium (*orange shading*) and saturation (*blue shading*) ranges. The peak of the wave spectrum is k_p and the transition wavenumber is k_n. Panel *a* adapted with permission from Lenain & Pizzo (2020). (*b*) Whitecap coverage W_{CC} versus the wind speed at 10 m, U_{10}, from field measurements and modeled from the length distribution $\Lambda(c)$ (Romero 2019), with some empirical parameterizations indicated. The line labeled MOM1980 is designed to fit the historical data from Monahan & Muircheartaigh (1980). A large scatter in the data remains. (*c*) The length distribution $\Lambda(c)$ of crests moving at a speed *c* from field experiments (Kleiss & Melville 2010, Sutherland & Melville 2013, Schwendeman et al. 2014, Deike et al. 2017a), with scatter similar to the whitecap coverage in terms of the amplitude of $\Lambda(c)$. Note that the infrared measurements extend to the microbreaker range (*c* < 1 m/s), where air is not entrained. The spectral model from Romero (2019) is shown in colored lines and encompasses the variability observed in the field. (*d*) Rescaling the length distribution $\Lambda(c)$ in panel *c* according to Equation 12 significantly reduces the scatter in the data.

has proven challenging, and large scatter in the recent data set still remains when presented as a function of wind speed only, as shown in **Figure 4b**. The scatter is related to the dependency of breaking waves on the sea state, to the local breaking intensity, to the details of the image processing, and to the possible role of temperature and water contamination on the lifetime of bubble plumes (Callaghan et al. 2008, 2017; Kleiss & Melville 2010; Schwendeman & Thomson 2015; Brumer et al. 2017b). Since the whitecap coverage provides only geometric information, relationships to the local wave field are made empirically. Nevertheless, once provided with a measure or model of W_{CC}, one can propose empirical relationships with the related bubble gas flux or production of sea sprays by bubbles (Lewis & Schwartz 2004, Garbe et al. 2014, de Leeuw et al. 2011).

3.2.2. The length distribution of breaking crests and the Phillips (1985) framework.

Phillips (1985) introduced the length distribution of breaking crests, $\Lambda(\mathbf{c})$, with $\Lambda(\mathbf{c})\,d\mathbf{c}$ the expected length of breaking crests moving between $\mathbf{c}$ and $\mathbf{c} + d\mathbf{c}$ (per unit ocean surface area). The azimuth-integrated length distribution is $\Lambda(c) = \int \Lambda(\mathbf{c})c\,d\theta$. This scale-by-scale representation of the breaking field tracks the breaking fronts and their speeds (see **Figure 1**). The role of breaking waves in air–sea fluxes is then naturally obtained through the moments of $\Lambda(\mathbf{c})$. The zeroth moment gives the total length of breaking fronts (per unit ocean surface area), $L = \int \Lambda(\mathbf{c})\,d\mathbf{c}$. The first moment gives the fraction of total surface area turned over per unit time, $R = \int c\Lambda(\mathbf{c})\,d\mathbf{c}$. The whitecap coverage is dimensionally given by $W_{CC} = \int \tau c\Lambda(\mathbf{c})\,d\mathbf{c}$, where τ is the characteristic whitecap lifetime, which can be related to the breaking scales by $1/\tau \propto ck$, which leads to the second moment, $W_{CC} \propto \int c^2 \Lambda(\mathbf{c})\,d\mathbf{c}$. This formulation naturally contains sea state variability of the whitecap coverage through the sea state variability of the $\Lambda(c)$ distribution (Kleiss & Melville 2010, Romero 2019). The fourth moment relates to the momentum flux, while the fifth moment gives the energy dissipation due to breaking waves per unit surface area,

$$M = \int \frac{b\rho}{g}c^4\Lambda(\mathbf{c})\,d\mathbf{c}, \quad S_{\text{diss}} = \int \frac{b\rho}{g}c^5\Lambda(\mathbf{c})\,d\mathbf{c}, \qquad 11.$$

where b is the breaking parameter [see Section 2, Duncan (1981), and Phillips (1985)].

The breaking parameter has been shown to depend on the breaking slope (Section 2). Romero et al. (2012) proposed to estimate the local slope from the saturation spectrum, $S = bk \equiv \sqrt{B(k)} = \sqrt{\phi(k)k^3}$, to obtain a spectrally defined breaking parameter $b(k) = A_T[\sqrt{B(k)} - \sqrt{B_T}]^{5/2}$, where A_T is a nondimensional coefficient and B_T is a breaking threshold. The coefficients A_T and B_T have orders of magnitude constrained by laboratory experiments and values adjusted to balance the wind input term used in spectral models (Romero et al. 2012, Romero 2019). Sutherland & Melville (2013, 2015) measured the turbulent kinetic energy using acoustic sensors jointly with energy dissipation by breaking waves estimated from remote sensing of the breaking distribution. This demonstrated that the $\Lambda(c)$ framework allows one to close the energy and momentum budget under a breaking wave field.

Following work by Longuet-Higgins (1957), Romero & Melville (2011) and Romero (2019) related the breaking statistics to the wave spectrum by assuming proportionality between the breaking statistics and the statistics of crest lengths exceeding a wave slope criterion. The breaking statistics in the k-space is then written as $\Lambda(\mathbf{k}) = \frac{l}{k}\exp(-B_{\text{br}}/B(\mathbf{k}))M_L(\mathbf{k})M_W(k)$, where $M_W(k)$ is a wind modulation function, accounting for the amplification of the short waves to balance the wind input; $M_L(k)$ is a function accounting for the breaking modulation by the longer waves; and B_{br} is a breaking threshold parameter. Romero (2019) used this within spectral wave models and obtained a modeled distribution of the breaking statistics that is fully compatible with field

measurements of $\Lambda(c)$ and realistic whitecap coverage, validating this spectral modeling approach (see **Figure 4c,d**).

3.2.3. Measuring and scaling $\Lambda(c)\,dc$.

Phillips (1985) proposed dimensional arguments to describe the shape of the breaking distribution based on an equilibrium between energy dissipation and wind input, leading to $\Lambda(c) \propto g u_*^3 c^{-6}$.

The potential of the $\Lambda(c)$ framework to estimate the energy, momentum, and mass transfer between the ocean and the atmosphere has motivated measurements using infrared and visible cameras on research vessels/platforms (Gemmrich et al. 2008, Thomson et al. 2009, Zappa et al. 2012, Sutherland & Melville 2013, Schwendeman et al. 2014) and from aircraft (Kleiss & Melville 2010, Deike et al. 2017a) with discussion of the processing methodologies (Banner et al. 2014). Overall, these field measurements have confirmed the $\Lambda(c) \propto c^{-6}$ scaling over a wide range of scales, while also highlighting a more complex dependency on fetch and wave age (see **Figure 4c**). Sutherland & Melville (2013) proposed the scaling

$$\frac{\Lambda(c)c_{\rm p}^3}{g} = \hat{K}\left[\frac{c}{\sqrt{gH_{\rm s}}}\left(\frac{gH_{\rm s}}{c_{\rm p}^2}\right)^{1/10}\right]^{-6}\left(\frac{u_*}{c_{\rm p}}\right)^{1/2},$$

with $\hat{K} \approx 0.05$ a nondimensional constant fitted to the data. A key success in this result has been to rescale c by $\sqrt{gH_{\rm s}}$, a characteristic speed accounting for the breaking strength, which is inspired by the scales of turbulent motion under breaking waves (see Section 2). Deike & Melville (2018) pointed out the weak $(gH_{\rm s}/c_{\rm p}^2)^{1/10}$ dependency and used the fetch-limited relationship, $gH_{\rm s} \propto c_{\rm p}^2$, to propose a simplified scaling,

$$\frac{\Lambda(c)\sqrt{gH_{\rm s}}^3}{g} = K\left(\frac{c}{\sqrt{gH_{\rm s}}}\right)^{-6}\left(\frac{u_*}{\sqrt{gH_{\rm s}}}\right)^{5/3}, \qquad 12.$$

where $K \approx 0.25$ is a fitted nondimensional constant, which is shown in **Figure 4d** to collapse all data within an order of magnitude.

3.3. Air Flux over an Ensemble of Breaking Waves

We now consider the air bubble flux into the water associated with breaking, combining the breaking distribution and the individual entrainment described in Section 2. This is central to the scale-dependent estimation of bubble-mediated gas flux and sea spray generation by bubble bursting. Deike et al. (2017a) defined the rate of entrainment of air per unit area of ocean surface V_A (in units of a volume per area per time) as

$$V_A = \int v_l(c)\Lambda(c)\,dc, \text{ with } v_l(c) = V/(L_c\tau_b), \qquad 13.$$

where $v_l(c)$ is the volume of air entrained by breakers moving at a speed between c and $c + dc$, per unit time, per unit length of breaking crest. It is given by the volume of air entrained by a single breaker V (Equation 7) and by the plume lifetime $\tau_b \propto b/W$, so that we have

$$V_A = \int B \frac{b}{(bk)}\frac{c^3}{g}\Lambda(c)\,dc. \qquad 14.$$

The volume of air entrained by breaking waves (which is the volumetric analog of the whitecap coverage) is therefore given by the third moment of $\Lambda(c)$, modulated by a factor that depends on the breaking strength, as well as by the ratio of work done by buoyancy forces and mechanical

dissipation. Using Equation 3, we have $V_A = \int B s(k)^{3/2} \frac{c^3}{g} \Lambda(c)\, dc$, with $s(k) \approx hk$, and following the work done on energy dissipation, we consider $b/hk = s(k)^{3/2} = A_T(\sqrt{k^3 \phi(k)} - \sqrt{B_T})^{3/2}$ using the same constants A_T and B_T as for energy dissipation.

The volume flux V_A can then be estimated by knowledge of the breaking statistics $\Lambda(c)$ and wave spectrum $\phi(k)$, for any wave state, in the presence of swells and wind waves. Note that open-ocean measurements of the volume flux under breaking waves are extremely challenging, and a direct validation of Equation 14 in the field is lacking. This formulation of the total air bubble flux will be validated a posteriori when considering the associated gas and sea spray fluxes (involving other assumptions and models) in Sections 4 and 5.

k_w: the gas transfer velocity, which measures the transport of gas between the ocean and the atmosphere

4. FROM THE ATMOSPHERE TO THE OCEAN: BUBBLE-MEDIATED GAS TRANSFER

4.1. Challenges in Estimating the Gas Transfer Velocity

Gas transfer at the ocean surface is of paramount importance, with ocean uptake accounting for about 30% of the carbon dioxide (CO_2) released into the atmosphere (Friedlingstein et al. 2020) and air bubbles entrained by breaking waves accounting for about 40% (Reichl & Deike 2020), while bubbles dominate the gas transfer of low-solubility gases such as O_2, which is key to biological activity (Emerson et al. 2019). The gas transfer between the ocean and the atmosphere is usually represented as (Wanninkhof et al. 2009)

$$F = k_w(C_0 - C_a) = k_w(C_0 - K_0 p_a), \qquad 15.$$

with k_w the gas transfer velocity and $C_0 - C_a$ the concentration difference between the ocean (C_0 is the concentration in the well-mixed bulk) and atmosphere (C_a is the concentration in the air at the surface), the latter of which is sometimes written in terms of the gas partial pressure p_a (kg m^{-1} s^{-2}) and the gas solubility in seawater K_0 (mol s^2 kg^{-1} m^{-2}). The gas transfer velocity can be measured by dual-tracer (Ho et al. 2006, 2011) and eddy covariance techniques (Edson et al. 2011, Bell et al. 2017, Brumer et al. 2017a), and there are extensive reviews on field measurements by Wanninkhof et al. (2009) and Garbe et al. (2014). Traditional parameterizations used in ocean and climate models (e.g., Liss & Merlivat 1986; Wanninkhof 1992, 2014; Wanninkhof & McGillis 1999; Nightingale et al. 2000; Ho et al. 2006, 2011; Wanninkhof et al. 2009) for the gas transfer velocity k_w reflect a correlation with wind speed, $k_w^{W14} = C_{W14} U_{10}^2 (Sc/660)^{-1/2}$, where $Sc = \nu/D$ is the Schmidt number (which compares the water kinematic viscosity ν to the gas diffusivity D), U_{10} is the wind speed at 10 m, and C_{W14} is an empirical constant constrained using bulk field observations, global inventories, and tracer budget experiments (Wanninkhof et al. 2009, Wanninkhof 2014). The power dependence on U_{10} (here quadratic) is an empirical result taken when considering mean wind speed dependence in field studies and is supposed to encompass the role of turbulence and bubbles in increasing the transfer velocity at high wind speed. The transfer velocity is often given relative to $Sc = 660$, the value of Sc for CO_2 in seawater at 20°C: $k_{w660} = k_w(\frac{Sc}{660})^{1/2}$. As shown in **Figure 5a**, recent open-ocean gas transfer velocity measurements of CO_2 and dimethylsulfide (DMS) display very large scatter when analyzed as a function of wind speed (Miller et al. 2009, Edson et al. 2011, Bell et al. 2017, Brumer et al. 2017a, Leighton et al. 2018), exposing the failure of wind speed parameterization at intermediate to high wind speeds associated with bubble-mediated gas transfer. Woolf et al. (2019) summarized the remaining uncertainties in the global carbon uptake by the ocean as coming from uncertainties in spatial measurements of the partial pressure difference and in modeling the gas transfer velocity.

Separating the contribution to the total flux into the bubble gas transfer and the diffusive transfer at an unbroken surface, bubble-mediated gas transfer has been introduced as a function of the whitecap coverage (Woolf & Thorpe 1991, Keeling 1993, Woolf 2005). The COAREG (Coupled Ocean–Atmosphere Response Experiment Gas transfer algorithm) framework, a sophisticated model that uses such decomposition, has been widely used to reproduce field measurements (Fairall et al. 2003, Edson et al. 2011, Bell et al. 2017). However, all the wave information is lost when considering the whitecap coverage empirical formulation with wind speed, which limits comparisons between different sea state configurations and is hidden in the uncertainties of the coefficients in COAREG. In an effort to collapse available field data, parameterizations using wind speed and significant wave height have been proposed, with empirical coefficients for CO_2 and DMS, that show a reasonable collapse of the data (Brumer et al. 2017a). Another effort is to use the turbulence dissipation rate in the water as a better proxy for gas transfer (Esters et al. 2017).
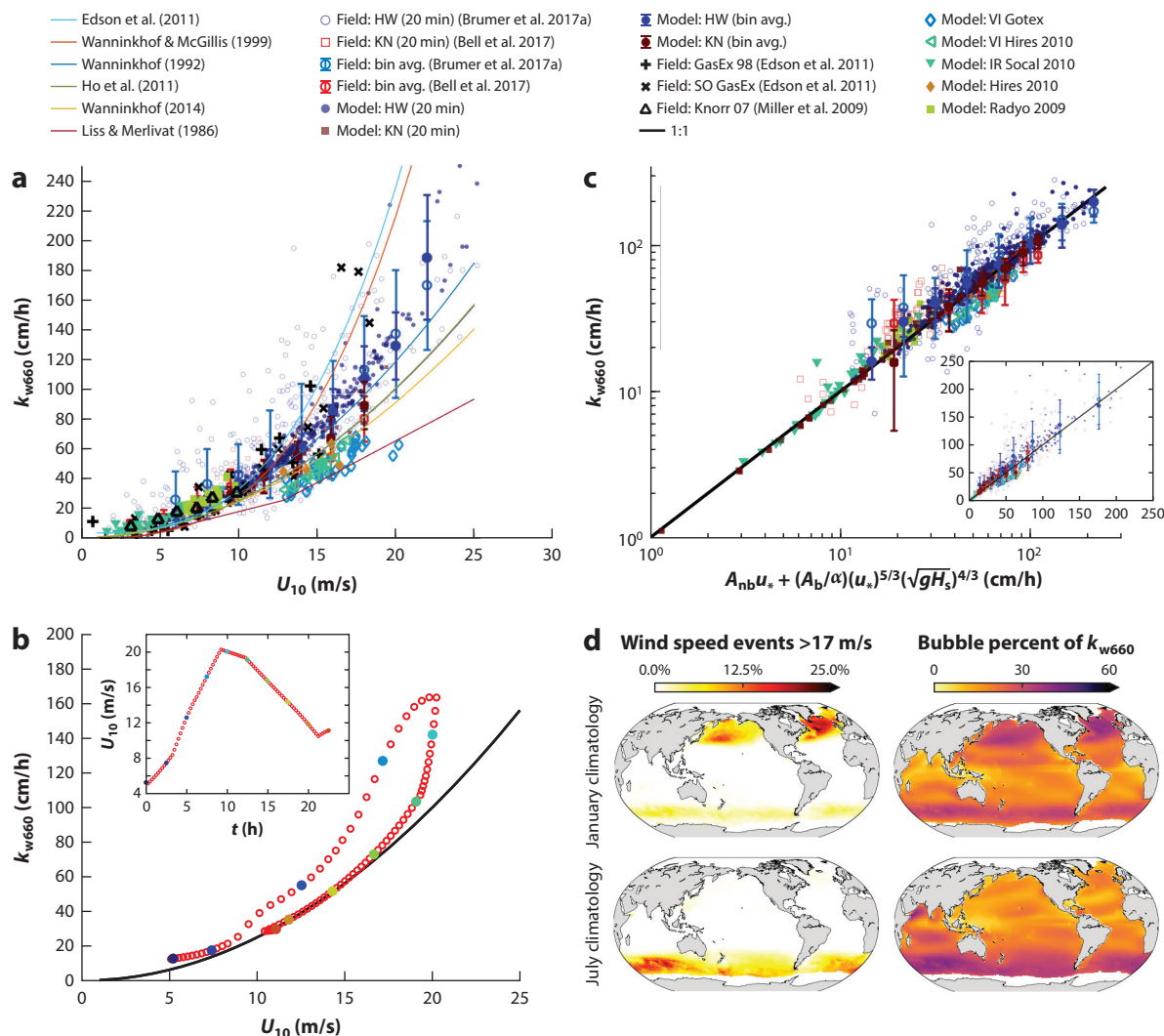
(*Caption appears on following page*)

Figure 5 (*Figure appears on preceding page*)

(*a*) Gas transfer velocity for CO_2, k_{w660}, as a function of the wind speed at 10 m, U_{10}, for multiple field campaigns (*symbols*) and wind-only quadratic and cubic parameterizations (*curves*). A large scatter in the data is observed. Data from Brumer et al. (2017a) and Bell et al. (2017) appear as open blue circles and red squares, respectively, and the modeled data (Equation 21; Deike & Melville 2018) for these conditions are shown as filled blue circles and red squares, with the thinner symbols representing 20-min-averaged data and the bold symbols with error bars representing data bin averaged with wind speed. Solid lines are various empirical relationships based only on wind speed found in the literature: (*top* to *bottom*) Edson et al. (2011), Wanninkhof & McGillis (1999), Wanninkhof (1992), Ho et al. (2011), Wanninkhof (2014), and Liss & Merlivat (1986). Deike & Melville's (2018) model reproduces the field measurements with good accuracy given the complexity of the processes. The Gotex model is modeled data from Deike & Melville (2018) based on data described by Kleiss & Melville (2010), and Hires 2010, Radyo 2009, and Socal 2010 are modeled data from Deike & Melville (2018), based on field campaign conditions from Sutherland & Melville (2013). (*b*) Spectral gas transfer velocity k_{w660} (Equation 21) during a single 24-h storm in the Southern Ocean modeled using WW3 (original data), illustrating sea state–induced variability on the gas transfer velocity, with a difference up to a factor of two at the same wind speed between the storm intensification stage and the set-down. (*Inset*) Wind speed U_{10} as a function of time. The colored markers indicate the time evolution across storm intensification and set-down. (*c*) Semiempirical formulation (Equation 23) for the gas transfer velocity for CO_2 and DMS, $k_{w660} = A_{nb}u_* + (A_b/\alpha)(u_*^{5/3})(\sqrt{gH_s})^{4/3}$, with $A_b = \tilde{A}_b(Sc/660)^{1/2}$, where $\tilde{A}_b = 1.1 \pm 0.3 \times 10^{-5}$ m^{-2}s^2 is the only fitted parameter. The main figure is log scaled while the inset is linearly scaled and displays a good collapse of the data (Deike & Melville 2018). (*d, right*) Contribution of bubble gas transfer velocity obtained using global WW3 simulations and Equation 23 that have been averaged across January (*top right*) and July (*bottom right*) over 30 years (1985–2015), showing that bubbles account for up to 50% of the k_{w660} for CO_2 at high latitudes in winter, (*left*) corresponding to a high frequency of wind speed events over 17 m/s. Panels *a* and *c* adapted with permission from Deike & Melville (2018); panel *d* adapted with permission from Reichl & Deike (2020). Abbreviations: avg., average; DMS, dimethylsulfide; HW, HiWinGS campaign; IR, infrared camera data; KN, Knorr 2011 campaign; SO GasEx, Southern Ocean Gas Exchange experiment; VI, visible camera data; WW3, WAVEWATCH III.

The case of low-solubility gases, for which the bubble-mediated gas transfer is even more important (Keeling 1993, Emerson & Bushinsky 2016, Leighton et al. 2018), is especially challenging given the separate role of large and small bubbles, the latter bringing an asymmetric contribution (Woolf & Thorpe 1991, Leighton et al. 2018). There is currently no consensus on the formulation of the gas transfer velocity to be used in large-scale models for O_2 and N_2. Atamanchuk et al. (2020) recently showed that using different models for k_w leads to variations in orders of magnitude and even a change of the sign of the flux in certain high–wind speed events, which is linked to the representation (or the lack thereof) of the asymmetric bubble contribution. As such, significant disagreements remain between empirical formulations and field measurements of N_2 and O_2 fluxes (Stanley et al. 2009, Emerson & Bushinsky 2016, Liang et al. 2017, Emerson et al. 2019, Atamanchuk et al. 2020).

4.2. Gas Transfer Velocity

The present section discusses bubble-mediated transfer models and their integration within a sea state–dependent gas transfer velocity formulation. We start by writing the flux as (Woolf & Thorpe 1991, Keeling 1993)

$$F = F_{nb} + F_b, \qquad \qquad 16.$$

separating the nonbreaking, F_{nb}, and bubble-mediated, F_b, gas flux contributions.

4.2.1. Unbroken flux and gas transfer velocity. The nonbreaking contribution F_{nb} is driven by diffusive mass transfer at the unbroken air–sea interface, which is enhanced by turbulence. Following eddy renewal theory, F_{nb} scales with $Sc^{-1/2}$ and scales linearly with the friction velocity u_* (Garbe et al. 2014):

$$F_{nb} = k_{nb}(C_0 - C_a), \text{ with } k_{nb} = A_{nb}u_*\left(\frac{Sc}{660}\right)^{-1/2}. \qquad 17.$$

The nondimensional coefficient A_{nb} is empirical and varies by about 20–30% in the literature, depending on whether CO_2 or DMS data at relatively low wind speed are used as constraints (Fairall et al. 2003, Woolf 2005, Edson et al. 2011). The scaling in friction velocity is equivalent to the one involving the turbulent dissipation rate, $k_{nb} \propto Sc^{-1/2}(\nu\varepsilon)^{1/4}$ (Zappa et al. 2001, Garbe et al. 2014). While the turbulence is a more direct controlling factor of the gas transfer than the friction velocity, systematic measurements just below the free surface remain challenging. Note also that the unbroken transfer could depend on the surface wave conditions, which could be estimated through the turbulence dissipation term or via a sea state–dependent drag coefficient C_D that links the wind speed at 10 meters and the friction velocity.

4.2.2. Bubble gas transfer models. The bubble flux F_b can be written as the sum of two terms, one representing bubbles with the ability to flux in or out depending on the concentration gradient, written as $k_b(C_0 - C_a)$, where k_b is the bubble gas transfer velocity. The second term represents the asymmetric pathway from small bubbles fully dissolving in the water column. The size cutoff for these small bubbles is estimated to be between 50 and 300 μm depending on the models, which corresponds to bubbles that have rise velocities smaller than the water turbulence fluctuations and, hence, are not able to rise back to the surface but instead eventually collapse due to hydrostatic and surface tension pressure.

Woolf & Thorpe (1991) proposed the model $F_b = -k_b[C_a(1 + \delta) - C_0]$, with δ the asymmetric contribution. Breaking waves directly control the bubble gas transfer velocity through air entrainment and earlier formulations have used the whitecap coverage as a large-scale constraint, with $k_b \propto W_{CC}$. The bubble dynamics in the upper turbulent ocean is then treated in a Lagrangian way, with various levels of complexity. It involves an injected bubble size distribution $Q(R_b)$ and a modeled bubble rise velocity $w_b(R_b)$, together with an individual gas transfer bubble velocity $\kappa_b(R_b)$. The upper-ocean dynamics is modeled through its background turbulence velocity and can account for idealized Langmuir circulation in order to consider deeper entrainment of small bubbles (Leighton et al. 2018). As discussed by Emerson & Bushinsky (2016), Liang et al. (2017), Leighton et al. (2018), and Emerson et al. (2019), the asymmetric pathway is especially important for low-solubility gases like N_2 and O_2 but has also been proven to be important at high wind speed for CO_2 (Leighton et al. 2018).

The gas exchange model from Woolf & Thorpe (1991) has been recently combined with LES of the upper ocean (Liang et al. 2011, 2012, 2017), including the stochastic forcing resulting from realistic breaking wave statistics (Liang et al. 2017). This formulation has provided the most detailed description of the role of bubbles in storms for CO_2, N_2, and O_2 and has demonstrated the nontrivial role of bubbles in enhancing or limiting gas exchange, together with nonlinear hysteresis cycles when wind speed increases or decreases (Liang et al. 2017). This approach presents the key advantage of integrating complex upper-ocean processes such as entrainment of bubbles by Langmuir circulation to greater depths, which would result in much longer residence times (Liang et al. 2012). The downside is that the full sea state–dependent LES requires high-resolution computations, which are usually too expensive to extend to ocean scales and limit the assessment of the importance of gas exchange sea state variability on large-scale and long-term patterns.

The original bubble-mediated gas model from Keeling (1993) also separated the contribution of small and large bubbles, with the flux written as

$$F = F_{nb} + F_b = (k_{nb} + k_b)(C_0 - K_0 p_a) + k_b^{asym} K_0 p_a. \qquad 18.$$

Keeling (1993) discussed the resulting supersaturation for major gases, while arguing that large bubbles are important for CO_2 gas exchange. The contribution of large bubbles is related to the total air bubble flux, $k_b = \int dR_b \, (4\pi/3) R_b^3 Q(R_b) E(R_b)/\alpha$, where $E(R_b)$ is a size-dependent efficiency

coefficient that estimates in an integrated way the amount of gas transferred by each bubble, $Q(R_b)$ is the bubble flux, and α is the (nondimensional) Ostwald gas solubility. Keeling (1993) estimated the entrained volume flux $V_A = \int dR_b\,(4\pi/3)R_b^3 Q(R_b)$ from the whitecap coverage $V_A \propto W_{CC}$. The efficiency coefficient was written in terms of the depth of bubble injection z_0 and an equilibration depth $H_{eq}(R_b)$,

$$E(R_b) = \frac{z_0}{z_0 + H_{eq}(R_b)} \text{ and } H_{eq}(R_b) = \frac{4\pi}{3\alpha}\frac{R_b w_b(R_b)}{\kappa_b(R_b)}, \qquad 19.$$

where $\kappa_b(R_b)$ is the individual bubble exchange rate with the surrounding water and z_0 is the bubble injection depth. These equations provide a depth-integrated estimation of the gas exchange by bubbles within a turbulent background. The equilibrium depth $H_{eq}(R_b)$ can be interpreted as the depth at which the bubble will exchange all of its gas content. This formulation is simple once it is provided with accurate models of the input bubble size distribution, rise velocity, individual exchange coefficient, and injection depth.

The asymmetric term was written as $k_b^{asym} K_0 p_a$ (Keeling 1993) and expressed as $k_b^{asym} = V_{inj}/\alpha + \Delta P/P_0 \int dR_b\,(4\pi/3)R_b^3 Q(R_b)E(R_b)/\alpha$, where V_{inj} is the volume of the small bubbles, which are assumed to completely dissolve. The second term is related to the average depth of the bubble plume and can be written as $\Delta P/P_0 \int dR_b\,(4\pi/3)R_b^3 Q(R_b)E(R_b)/\alpha = \int dR_b\,(4\pi/3)R_b^3 Q(R_b)F(R_b)/\alpha$, with $F(R_b) = \frac{H_{eq}}{H_0}\frac{z_0^2}{[z_0+H_{eq}(R_b)]^2}$. The gas supersaturation can also be estimated from this model (see Keeling 1993).

4.2.3. Bubble model input: injection depth, rise velocity, and transfer rate in turbulence.

All bubble-mediated gas transfer models require information on the injection depth z_0, rise velocity $w_b(R_b)$, and individual bubble exchange rate $\kappa_b(R_b)$. The rise velocity and individual transfer rates derived for bubbles moving in quiescent flow have been used for clean and contaminated (dirty) interfaces (Woolf & Thorpe 1991, Keeling 1993, Levich 1962). However, bubbles entrained by breaking will be subject to a turbulent flow, modifying their velocity and transfer rate. I briefly summarize some results of this vast topic, which stresses the role of turbulent fluctuations on the bubble residence time and individual gas exchange velocity and should be integrated to air–sea bubble gas exchange models.

The injection depth can be estimated as the breaking height, $z_0 \sim h$, which is supported by laboratory experiments and simulations (Lamarre & Melville 1991, Deane & Stokes 2002, Callaghan et al. 2013, Deike et al. 2016), as well as some field measurements (Bowyer 2001, Lenain & Melville 2017a). We note the difficulty in measuring bubbles next to the surface in the field, which deserve further measurements, along with breaking observations.

The rise of bubbles in a turbulent background remains poorly understood, as there are size-dependent effects of the turbulent background on the drag and lift forces of the bubbles. Most experimental and numerical studies have reported a slowdown compared to the rise velocity in quiescent water, varying from 20 to 70%, mainly controlled by the relative intensity of the turbulent fluctuations u_{rms} and the quiescent bubble velocity, while complex coupling with the mean flow limits comparisons between data sets (Poorte & Biesheuvel 2002, Aliseda & Lasheras 2011, Salibindla et al. 2020, Ruth et al. 2021).

The turbulent flow surrounding the bubbles modifies the individual bubble diffusive gas exchange by changing the characteristic timescale of eddy renewal, $\tau_t \propto R_b/\tilde{w}$, where $\tilde{w}$ is a turbulent velocity (either the rise velocity in turbulence or the turbulent fluctuations u_{rms}), leading to a transfer rate $\kappa_b \propto \sqrt{D\tilde{w}/R_b}$, which is similar to the result in quiescent water but now accounts for a turbulent velocity (Farsoiya et al. 2021).

4.3. Sea State–Dependent Bubble-Mediated Gas Transfer Velocity

Deike & Melville (2018) combined the description of air entrainment and bubble population discussed in Sections 2 and 3 with the model from Keeling (1993) to account for the sea state effects on the bubble-mediated gas transfer velocity k_b (but did not consider asymmetric effects). The bubble-mediated transfer is controlled by the size distribution of bubbles being entrained (written as a number per unit ocean surface area per unit time),

$$Q(R_b) = \int q_l(R_b, c)\Lambda(c)\,dc, \text{ with } q_l(R_b, c) = \frac{B}{2\pi}s(k)^{3/2}N(R_b)\frac{c^3}{g}, \qquad 20.$$

where $q_l(R_b, c)$ is the size-dependent bubble flux per unit length of a breaking crest. The bubble size distribution $N(R_b)$ is described in Section 2. For bubbles R_b larger than the Hinze scale R_H that contain 95% of the volume, we have $N(R_b) \propto R_b^{-10/3}$, while for $R_b < R_H$, we have $N(R_b) \propto R_b^{-3/2}$, so that the total volume of air entrained is given by the large-scale constraints on the total volume flux, Equation 14, and $0.95V_A = \int_{R_H}^{R_M} dR_b Q(R_b)\frac{4\pi}{3}R_b^3$. The bubble gas transfer velocity k_b is then written as (Deike & Melville 2018)

$$k_b = \iint dc\,dR_b\,f_l(R_b, c)\Lambda(c), \text{ with} \qquad 21.$$

$$f_l(R_b, c) = \frac{q_l(R_b, c)E(R_b)}{\alpha}\frac{4\pi R_b^3}{3} = \frac{B}{2\pi}\frac{s(k)^{3/2}c^3}{g}\frac{4\pi R_b^3}{3}\frac{N(R_b)E(R_b)}{\alpha}. \qquad 22.$$

This equation yields a bubble gas transfer velocity that combines the bubble-mediated transfer estimated from the physicochemical properties of the gas (solubility, diffusivity, and viscosity) with the wave and wave breaking statistics.

A mechanistic understanding of the sea state variability can then be explored by considering a spectral wave model, such as WAVEWATCH III (WW3) (Ardhuin et al. 2010) to simulate the wave spectrum, combined with the breaking modeling from Romero (2019) to compute $\Lambda(c)$ from the wave spectrum and the gas transfer model from Deike & Melville (2018), yielding the integration of Equation 22. We consider a typical winter storm in the Southern Ocean in **Figure 5*b***, with wind increasing from 5 to over 20 m/s in a few hours and significant wave height up to 7 m. We observe values of k_w up to a factor of two higher during the storm intensification period than during the set-down in the next 10 h, which rationalizes some of the observed variability in field measurements of k_w (shown in **Figure 5*a***). A systematic study of such hysteresis cycles and wave-induced high-frequency variability in the gas transfer velocity remains to be performed.

4.4. Simple Parameterization for Gas Transfer and Global Estimations

The large-scale ocean and climate communities widely use the classic wind-only formulations (e.g., Wanninkhof et al. 2009) and apply the results to other gases by considering only the role of the Sc number. This approach is insufficient, as demonstrated by various studies on low-solubility gases (Atamanchuk et al. 2020, Liang et al. 2017, Emerson et al. 2019) or for CO_2 during high-frequency storms (Leighton et al. 2018). However, the overhead in computational costs induced by a wave model coupled with large-scale ocean and climate models remains high. This motivates simple semiempirical formulations of the form $k_b = F(u_*, H_s, c_p, Sc, \alpha)$, which are valid for multiple gases, without having to retune the empirical coefficients. Such parameterizations could be used with wave climatology, as well as incoming satellite products [e.g., SWOT (Surface Water and Ocean Topography)], which will provide global coverage of the significant wave height H_s.

Deike & Melville (2018) proposed such a parameterization for the bubble-mediated gas transfer velocity, derived from Equation 22, as a function of u_* and H_s. It captures the main wave effect, as well as solubility and diffusivity, and collapses all available data for CO_2 and DMS, as shown in **Figure 5c** (but does not account for bubble asymmetric effects, which would be necessary for O_2 and N_2):

$$k_w^{simple} = k_{nb} + k_b^{simple}, \text{ with } k_b^{simple} = \left[\frac{A_B}{\alpha} \left(u_*^{5/3} \sqrt{gH_s}^{4/3} \right) \right] \left(\frac{Sc}{660} \right)^{-1/2}. \qquad 23.$$

Reichl & Deike (2020) used this formulation to estimate the potential role of sea state variability on gas transfer at the regional and global scales by running global wave simulations with WW3, combined with products reconstructing the CO_2 partial pressure difference. They estimated that the bubble-mediated CO_2 transfer accounts for about 40% of the total flux, with significant seasonal and regional variability, which dominates the gas transfer velocity at high latitudes in winter seasons due to the occurrence of multiple high–wind speed events, as illustrated by the monthly averaged maps in **Figure 5d**. The role of such sea state–dependent variability in global geochemical cycles remains to be tested, with potential implications for deeper water mass formation and composition.

5. FROM THE OCEAN TO THE ATMOSPHERE: SPRAY GENERATION BY BUBBLE BURSTING

Ocean spray is composed of small liquid droplets formed through two main pathways. Spume drops are produced from the tearing of breaking wave crests by strong winds (Veron et al. 2012, Ortiz-Suslow et al. 2016, Troitskaya et al. 2018, Erinin et al. 2019); this has recently been reviewed by Veron (2015) and I will not further discuss it here. The second drop-generation mechanism is bursting bubbles, which produces droplets via either film (Blanchard 1963, Lhuissier & Villermaux 2012) or jet drops (Spiel 1994, 1997; Ghabache et al. 2014; Deike et al. 2018), as sketched in **Figure 1c,d**. These droplets can then be transported to the upper atmosphere (Mueller & Veron 2009, Richter et al. 2019), where they may evaporate, affect the radiative balance of the atmosphere, and serve as cloud condensation nuclei (Lewis & Schwartz 2004, de Leeuw et al. 2011). The heat and momentum fluxes at the ocean–atmosphere interface are strongly modulated by sea spray and are major players in weather prediction and hurricane intensification (Veron 2015). These droplets transport water, heat, dissolved gases, salts, surfactants, and biological materials; their chemical compositions are affected by their production mechanisms and provide the chemical link coupling the ocean and the atmosphere (Prather et al. 2013, Cochran et al. 2017, Wang et al. 2017).

Despite the importance of sea spray aerosols, large uncertainties remain in predicting their size and velocity generation functions (Lewis & Schwartz 2004, de Leeuw et al. 2011, Veron 2015) due to the complexity of their formation and the large range of scales involved in the production processes, from bubbles bursting at the ocean surface to large-scale breaking waves. The role of the sea state is largely missing in classic parameterization of the sea spray generation function, while the role of the water contamination and enrichment by biological activity adds an extra layer of complexity, affecting the efficiency of bursting processes (Wang et al. 2017, Frossard et al. 2019, Néel & Deike 2021).

Here I present recent advances in our mechanistic understanding of the production of sea spray by bursting bubbles thanks to idealized laboratory and numerical simulations at the bubble scale, and I combine them with the description of the wave breaking dynamics (Section 2) and statistics

(Section 3). This leads to a physics-based sea spray generation function, which compares favorably with data and source functions from the literature.

5.1. Number and Size of Film and Jet Drops Produced by Bubble Bursting

Earlier studies [see reviews by Lewis & Schwartz (2004) and Veron (2015)] have identified the two mechanisms sketched in **Figure 1*c,d***. I focus on recent results describing the size, velocity, and number of drops ejected by bursting, driven by advances in high-speed photography and computational methods. The controlling parameters of jet and film drop production can be understood in terms of characteristic timescales and length scales, leading to a universal description of the ejection properties, which account naturally for variations in some ocean water properties. At the scales of drops and bubbles, capillary forces become dominant, and the influence of gravity can be evaluated by comparing the bubble scale R_b to the capillary length $\ell_c = \sqrt{\gamma/\rho g}$ (≈ 2.7 mm in water). Viscosity has a nontrivial role to play in selecting the capillary waves during the cavity collapse process and modulating the film drainage, so we introduce the viscocapillary length, $l_\mu = \mu^2/(\rho\gamma)$, which controls processes involving cavity collapse and jet formation (Eggers & Villermaux 2008).

5.1.1. Film drops. Film drops are generated by the puncture, retraction, and destabilization of the thin cap of bubbles usually larger than the capillary length, $R_b > \ell_c$. They are produced between $0.4 l_c$ and $3.8 l_c$ in tap water (Lhuissier & Villermaux 2012), which agrees with various work in salt water where film drops are observed from bubbles ranging from 1 to 10 mm (Cipriano & Blanchard 1981, Blanchard & Syzdek 1988, Resch & Afeti 1991). The retraction velocity of the film is given by the Taylor–Culick velocity, $V_{TC} = \sqrt{2\gamma/\rho h_b}$, where h_b is the film thickness at bursting. Lhuissier & Villermaux (2012) performed extensive laboratory experiments, illustrated in **Figure 6**, and provided a description of the film dynamics leading to its rupture, linking the film drainage and its associated broad-lifetime statistics. Once the film ruptures, the cap retracts and destabilizes, following a capillary-driven fragmentation pattern with the mean film drop size found to scale as $\langle r_d \rangle \propto R_b^{3/8} h_b^{5/8}$, varying from a few micrometers to 0.5 mm, as the film thickness h_b at rupture varies from 0.1 to ~ 50 μm (Lhuissier & Villermaux 2012). At a relative humidity of 80%, this leads to the smallest mean drop around $r_d^{80} \approx 1$ μm (using $r_d^{80\%} = 0.5 r_d$; note that drops smaller than the mean predicted value can still be produced). The mean number of film drops is described by $n_{film}(R_b) \propto (R_b/l_c)^2 (R_b/h_b)^{7/8}$ so that larger bubbles produce on average more film drops. The minimal film thickness in ocean water conditions is probably related to Marangoni instabilities that systematically lead to film rupture for h_b above 0.1 μm, while films fully covered by surfactants might reach smaller sizes (Néel & Villermaux 2018).

Separately, numerous measurements have reported solid dry particles (sea salt aerosols) with diameters down to 0.01 μm that have been attributed to film drops (Cipriano & Blanchard 1981, Resch & Afeti 1991, Mårtensson et al. 2003, Sellegri et al. 2006, Wang et al. 2017). Dry and liquid aerosol sizes are considered in the literature, depending on the type of measurements being performed. The conversion factor between dry solid salt particles and liquid droplets is usually $2D_d^{dry} = 2r_d^{80\%} = r_d$ (see Fitzgerald 1975, Lewis & Schwartz 2004). Below $D_d^{dry} \sim 0.1$ μm, sea spray aerosols are mainly of organic composition (Quinn et al. 2015, Bertram et al. 2018) and their sizes are not directly proportional to the liquid drop size, contrary to sea salt aerosols. As a consequence, the smallest liquid drop of 0.5 to 1 μm obtained from the theory of Lhuissier & Villermaux (2012) does not account for the smallest dry salt aerosol of 0.1 μm, and another theoretical scaling is necessary to properly predict the sub-micrometer aerosols.

Film drop production can be described by a coalescence-like fragmentation scenario (Villermaux 2020), leading to Gamma distribution of sizes. This distribution is a two-parameter
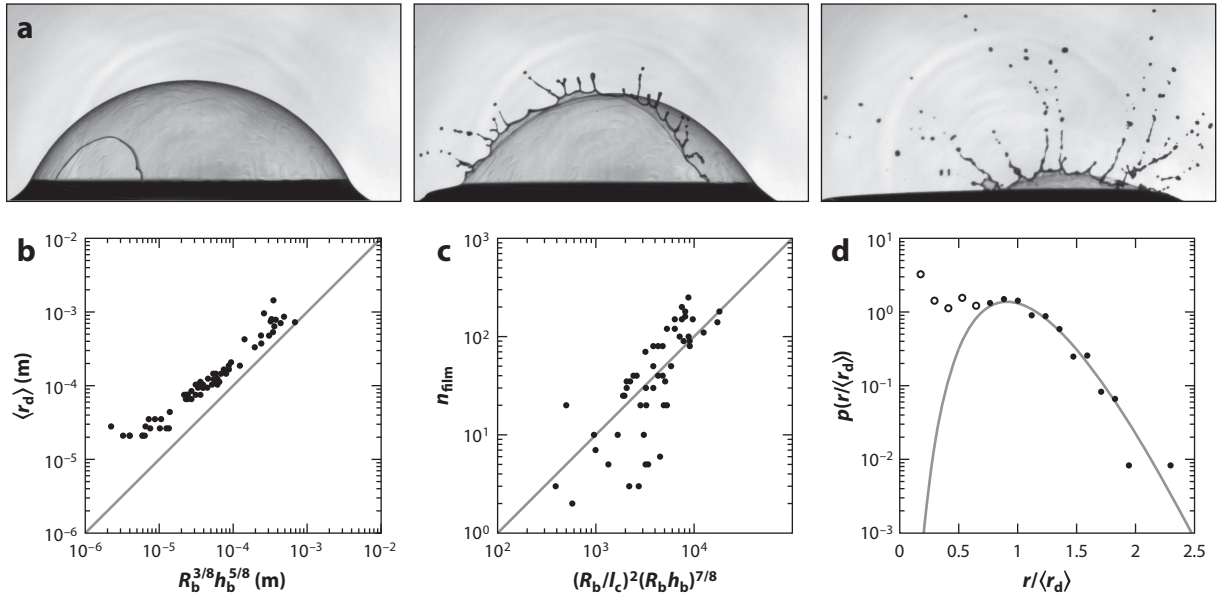
---

h_b: the thickness of a bubble's cap film at bursting, which controls film drop sizes

Dry and liquid aerosol sizes: the dry salt aerosol diameter D_d^{dry} can be related to the drop size at 80% humidity $r_d^{80\%}$ and the initial ejected liquid drop radius r_d by $2D_d^{dry} \approx 2r_d^{80\%} \approx r_d$

Figure 6

(*a*) The production of film drops by bubble bursting. (*b*) The resulting mean film droplet size as a function of the bubble radius and film thickness, $\langle r_d \rangle \propto R_b^{3/8} h_b^{5/8}$. (*c*) The number of film droplets produced as a function of bubble size, film thickness at bursting, and capillary length, $n_{film}(R_b) \propto (R_b/l_c)^2 (R_b h_b)^{7/8}$. (*d*) The size distribution of film droplets ejected by a bubble bursting event, described by a Gamma distribution (Equation 24) of order 11. Figure adapted with permission from Lhuissier & Villermaux (2012).

function controlled by the mean drop size $\langle r_d \rangle$ and its order m, which is controlled by the roughness of the ligaments during fragmentation [with $m = 11$ used to fit experimental data in Lhuissier & Villermaux (2012) and **Figure 6**]:

$$\mathcal{P}(r_d/\langle r_d \rangle) = \frac{m^m}{\Gamma(m)} \left(\frac{r_d}{\langle r_d \rangle} \right)^{m-1} e^{-m \frac{r_d}{\langle r_d \rangle}}. \qquad 24.$$

5.1.2. Jet drops. Jet drops are produced when the bubble cavity collapses and forms a vertical upward jet that destabilizes into drops. The cavity collapse is driven by the focusing capillary waves, leading to the jet ejection, with the wave propagation characterized by the inertio-capillary timescale $\tau_c = \sqrt{\rho R_b^3/\gamma}$, at the scale of the bubble radius R_b.

The use of high-speed cameras has led to very detailed and accurate experimental data of the jet drop production process (Ghabache et al. 2014, Ghabache 2015, Ghabache & Séon 2016, Brasz et al. 2018). Separately, Duchemin et al. (2002) presented the first DNS of the axisymmetric bubble bursting by solving for the two-phase Navier–Stokes equations and demonstrated that the main controlling parameter of the speed and size of the first ejected droplet is the ratio of the surface tension and viscous forces (as estimated by the Laplace or Ohnesorge number): $La = R_b/l_\mu = \frac{\rho \gamma R_b}{\mu^2}$. These simulations showed that there is an optimal Laplace number around 1,000 (about 20 μm for salt water at 20°C) for which jet focusing is most efficient and leads to the ejection of very fast tiny droplets [tens of meters per second for an $\mathcal{O}(1 \text{ μm})$ drop]. DNS, validated against laboratory data (Brasz et al. 2018, Deike et al. 2018, Berny et al. 2020) (see **Figure 7**), has further demonstrated the universal size and velocity of the first ejected droplet for a range of Laplace numbers from 900 to 100,000, which corresponds to the range of existence of jet drops in salt
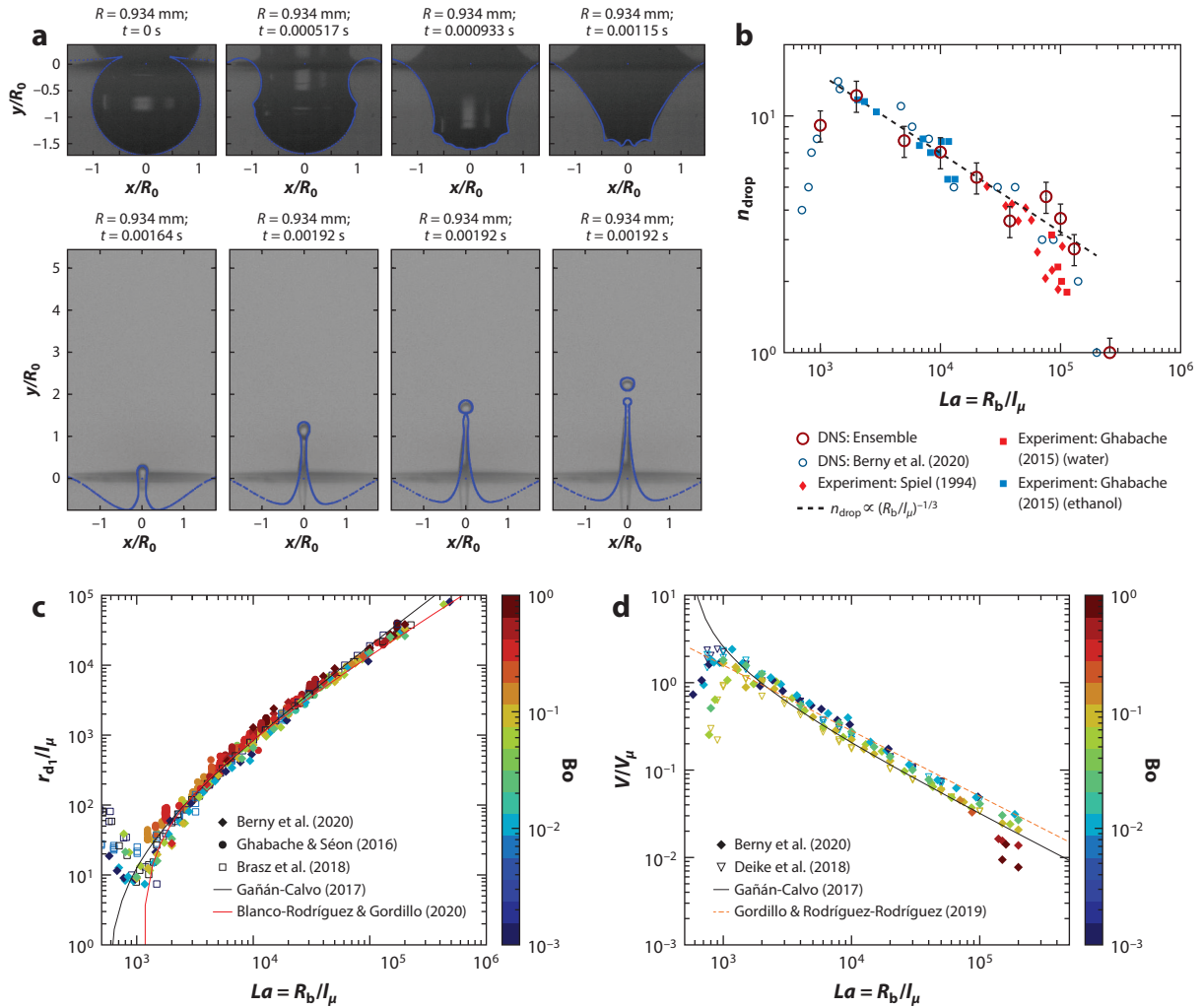
Figure 7

(*a*) An example of the jet drop dynamic from experiments (*photographs*) and direct numerical simulations (DNS) (*blue lines*) for a ∼1-mm bubble in water, which display excellent agreement in the cavity collapse and jet formation. Panel *a* adapted with permission from Deike et al. (2018). (*b*) The number of jet drops ejected n_{drop} as a function of $La = R_b/l_\mu$, with $l_\mu = \mu^2/(\rho\gamma)$. Drops are produced for $R_b/l_\mu > 600$, but not for $R_b^2/l_c^2 > 1$, with $l_c = \sqrt{\gamma/(\rho g)}$. (*c,d*) The size (*c*) and velocity (*d*) of the first jet drops as determined from experiments and simulations can be described by universal scalings (Equation 25), with excellent agreement between experiments and numerical simulations. Panels *b–d* adapted from Berny et al. (2020).

water for bubbles from 10 μm to 3 mm (at 20°C), with the jet and cavity following a self-similar inertio-capillary dynamic (Lai et al. 2018). The optimal Laplace number corresponds to the most effective focusing, with shorter (and slower) capillary waves damped by viscosity, so that the system is controlled by the fastest capillary wave. At higher R_b/l_μ (and higher R_b/l_c), the presence of several capillary waves leads to an imperfect focusing, slowing the jet formation and reducing the efficiency of drop production. These results inspired Gañán-Calvo (2017) to develop a set of scaling laws based on the momentum and energy balance during the cavity reversal process under the assumption that the key mechanism for ejection is the focusing of the most effective among

the fastest capillary waves produced by the retraction of the cavity. The first drop size r_{d_1} and velocity V_{d_1} are then given by (with $V_\mu = \gamma/\mu$)

$$\frac{V_{d_1}}{V_\mu} = k_v \left[La \left(La_\star^{-1/2} - La^{-1/2} \right) \right]^{-3/4} \quad \text{and} \quad \frac{r_{d_1}}{l_\mu} = k_r \left[\sqrt{La} \left(\sqrt{\frac{La}{La_*}} - 1 \right) \right]^{5/4}. \qquad 25.$$

In these scalings, $La_* \approx 550$ is the drop ejection threshold, while k_r and k_v are empirical $\mathcal{O}(1)$ constants fitted to the data. At high La, for the first drop (or jet) velocity, the asymptotic scaling is then $V_{d_1}/V_\mu \propto La^{-3/4}$, and for the first drop size the scaling is $r_{d_1}/l_\mu \propto La^{5/4}$. These scaling laws display excellent agreement with experimental and numerical data, for La from 900 to 10^6 (**Figure 7**), and illustrate a robust result: Knowing the bubble size and water properties, one can predict the first drop size and velocity through universal scalings of $La = R_b/l_\mu$, which encompass variations in temperature, salinity, density, viscosity, and surface tension. The physical assumptions behind these scalings have prompted ample discussions, and Gordillo & Rodríguez-Rodríguez (2019) and Blanco-Rodríguez & Gordillo (2020) have proposed an alternative theory based on capillary focusing, tracking the speed of the capillary waves during the cavity collapse, and an inertio-capillary balance, the final results of which describe the experimental and numerical data very well.

The production of jet drops is controlled by the ratio of the bubble size R_b to two characteristic lengths, l_μ and ℓ_c (Walls et al. 2015, Berny et al. 2020). For $R_b/\ell_c > 1$, drop ejection is prevented by the action of gravity, while the other limit for jet ejection is due to viscosity, which damps the waves during cavity collapse and prevents drop ejection for $R_b/l_\mu < 550$. For intermediate R_b/l_μ and R_b/ℓ_c, a nontrivial boundary exists (Walls et al. 2015) but is not relevant in sea water, as it corresponds to higher viscosities.

Thus, the lower bound for the production of jet drops is $R_b^{low}/l_\mu \approx 550$, with more efficient ejection above $R_b^{low}/l_\mu \approx 900$, which yields $10 < R_b^{low} < 30$ μm, depending on water temperature. Such bubbles create jet drops down to 0.5 μm in radius, which has been confirmed experimentally (Wang et al. 2017), so that in principle jet drops should not be disregarded when considering sub-micrometer production of sea spray aerosols (Wang et al. 2017, Berny et al. 2021).

Following Berny et al. (2020), Berny et al. (2021) used large ensembles of DNS to describe the statistics of jet drop ejection, characterizing the number and size of all jet drops produced when a cavity collapses. These results were validated against data from Spiel (1994, 1997), Ghabache et al. (2014), and Ghabache & Séon (2016) and showed that for salt water conditions, the mean number of jet drops follows $n_{jet}(R_b) \propto (R_b/l_\mu)^{-1/3}$ (so that smaller bubbles lead to more drops due to the capillary wave selection process, with a maximum of ~15 drops ejected). These simulations have shown that the mean drop size follows a scaling similar to that of the first drop (albeit simplified!), $\langle r_d \rangle \propto l_\mu (R_b/l_\mu)^{5/4}$. The drop size distribution of each ensemble can be approximated by a Gamma distribution (Equation 24) with a lower order, $m = 4$.

5.2. From a Single Bursting Bubble to the Sea Spray Droplet Distribution

The size distribution of drops produced by bursting bubbles entrained by a breaking wave is obtained by integration over all bubbles (Lhuissier & Villermaux 2012, Berny et al. 2021),

$$\mathcal{N}_d(r_d) = \int_{R_b^{low}}^{R_b^{up}} \frac{q(R_b) n(R_b)}{\langle r_d \rangle (R_b)} p(r_d/\langle r_d \rangle, R_b) \, dR_b, \qquad 26.$$

where $q(R_b)$ is the size distribution of bursting bubbles at the surface, and R_b^{low} and R_b^{up} are respectively the lower and upper bounds of the bubble radii able to produce drops through the considered mechanism. We assume that we can use the single–bubble bursting results from

La: the bubble Laplace number, which controls the size, velocity, and number of jet drops through the selection of the capillary waves during the cavity collapse; $La = R_b/l_\mu = \rho\gamma R_b/\mu^2$

Section 5.2 and the bubble size distribution under breaking waves from Section 2. Defining $\tilde{\alpha}$ and $\tilde{\beta}$ such that we have $q(R_b)n(R_b) \propto R_b^{-\tilde{\alpha}}$, $\langle r_d \rangle \propto R_b^{\tilde{\beta}}$, and $\zeta = (\tilde{\alpha} - 1)/\tilde{\beta}$, we integrate Equation 26 to obtain (Lhuissier & Villermaux 2012)

$$\mathcal{N}_d(r_d) = \mathcal{A} r_d^{-1-\zeta} \left[\Gamma_{inc}(m + \zeta, m r_d/r_d^{up}) - \Gamma_{inc}(m + \zeta, m_d/r_d^{low}) \right], \qquad 27.$$

where Γ_{inc} is the incomplete Gamma function, with $r_d^{up} = \langle r_d \rangle(R_b^{up})$ and $r_d^{low} = \langle r_d \rangle(R_b^{low})$, and $\mathcal{A}$ is the combined prefactor of the various algebraic laws.

Lhuissier & Villermaux (2012) performed the integration for the film drop distribution, with $R_b^{low,film} \approx 1$ mm and $R_b^{up,film} \approx 10$ mm, so that film drops are produced by super–Hinze scale bubbles with $q(R_b) \propto R_b^{-10/3}$; hence, we have $\zeta = 3/4$ and, thus, $\mathcal{N}_d(r_d)^{film} \propto r_d^{-7/4}$.

Berny et al. (2021) performed the integration for the jet drop distribution, with $R_b^{up,jet} \approx l_c \approx 2.7$ mm, so that jet drops are mainly produced by sub-Hinze bubbles, with $q(R_b) \propto R_b^{-3/2}$; hence, we have $\zeta = 2/3$ and, thus, $\mathcal{N}_d(r_d)^{jet} \propto r_d^{-5/3}$. Note that, in principle, we have $R_b^{low}/l_\mu \approx 900$ (10–30 μm, depending on temperature), which would lead to sub-micrometer jet drops, but bubbles below 50–200 μm have a rise velocity of $\mathcal{O}(1\text{cm/s})$ and may never reach the surface due to the turbulent background flow.

5.3. Integration over Breaking Statistics and the Sea State–Dependent Sea Spray Source Function

Finally, we use the air flux of bubbles under breaking waves, defined as the number of bubbles per unit ocean surface area per unit time, $Q(R_b)$, which is related to the air volume flux V_A [Equations 14 and 20; see Deike et al. (2017a) and Deike & Melville (2018)], to propose a sea state–dependent sea spray source function resulting from bubble bursting.

We write the sea spray generation function $F_d(r_d)$, resulting from one of the two bursting mechanisms, as the integration either of the bubble flux distribution, $Q(R_b)$, with the bursting production function or of the distribution of drops produced by bubbles of sizes between R_b and $R_b + dR_b$, $G(r_d, R_b) dR_b = \frac{n(R_b)}{\langle r_d \rangle} p(r_d/\langle r_d \rangle) dR_b$. The function $G(r_d, R_b)$ translates a bubble distribution (in the bulk water) into a drop distribution (in the air). For now, we assume that all bubbles within the bounds considered burst in a way comparable to single–bubble bursting studies. This yields a sea spray source function F_d, defined as the number of drops per unit surface ocean area per unit time [same units as $Q(R_b)$], which is physically consistent with the existing literature on the sea spray generation function:

$$F_d(r_d) = \int Q(R_b) \frac{n(R_b)}{\langle r_d \rangle} p\left(\frac{r_d}{\langle r_d \rangle}\right) dR_b \qquad 28.$$

$$= \iint \frac{B}{2\pi} \frac{s(k)^{3/2} c^3}{g} \Lambda(c) \, dc \frac{N(R_b) n(R_b)}{\langle r_d \rangle} p\left(\frac{r_d}{\langle r_d \rangle}\right) dR_b. \qquad 29.$$

This naturally considers the sea state effects through the $\Lambda(c)$ distribution, controlling the number flux of bubbles $Q(R_b)$, while physicochemical controls of the droplet production are included within $G(r_d, R_b)$, $n(R_b)$, $\langle r_d \rangle(R_b)$, and $p(r_d/\langle r_d \rangle)$. The sea spray generation function for film and jet drops (between their drop size bounds) follows

$$F_d(r_d)^{film} \propto r_d^{-7/4} V_A \text{ and } F_d(r_d)^{jet} \propto r_d^{-5/3} V_A. \qquad 30.$$

Figure 8 shows the result of integrating Equation 29 for a 24-h storm in the Southern Ocean, modeled using WW3 (using the same conditions as those for the gas transfer velocity in Section 4). We use reasonable guesses for the bounds of production of film drops from bubbles
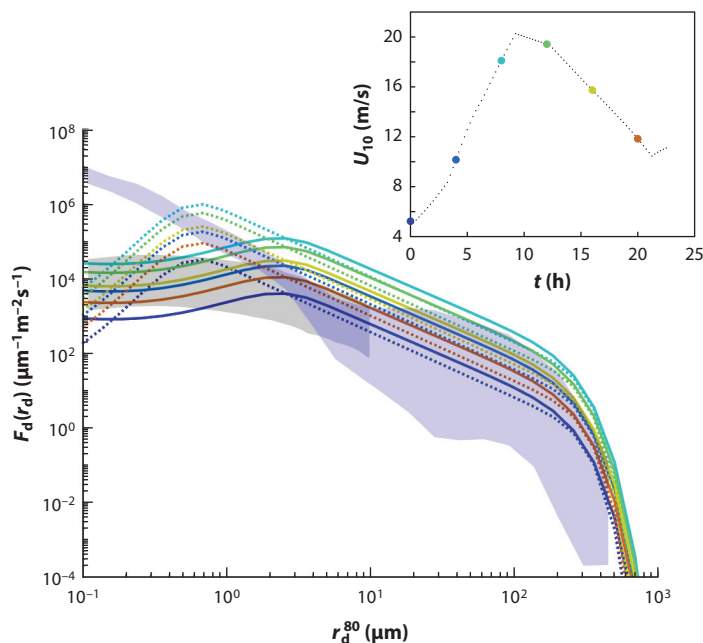
Figure 8

The sea spray generation function (SSGF) $F_d(r_d)$ (Equation 29) during a storm in the Southern Ocean. Solid lines indicate the jet drop production function, assuming the smallest bursting bubble is 50 μm in radius. Dotted lines indicate the film drop production function, assuming the peak radius of drops produced is 0.5 μm. Jet drops dominate above 2 μm in this representation. Radius is drop size at equilibrium at 80% relative humidity, $r_d^{80} = 0.5 r_d$. Colors indicate different times, with the corresponding wind speed at 10 m, U_{10}, shown in the inset, increasing from 5 m/s to 20 m/s over 10 h and then settling down, with more drops ejected during the storm intensification, corresponding to more intense breaking events. The light-blue area indicates the typical SSGF as summarized by Veron (2015) at 15 m/s, and the light-gray area indicates the typical SSGF as summarized by Lewis & Schwartz (2004) at 8 m/s. The sea state–dependent formulation falls within the uncertainties of previous empirical data and explains some of the variability previously reported.

(radii 1–10 mm) and for the minimal film thickness (0.1 μm), which leads to a drop size distribution peaking at 0.5 μm and with a maximum at 400 μm. Jet drops are considered for bubbles with radii from 50 μm to 2 mm, with a peak drop radius at 2 μm and a maximum at 800 μm. The prefactors for the drop productions are those suggested in **Figures 6** and **7**, following Lhuissier & Villermaux (2012) and Berny et al. (2021). In this representation, jet drops dominate the production above 2 μm, consistent with the earlier discussion by Woolf et al. (1987). This highlights the importance of understanding the bounds of production for jet and film drops, as both mechanisms are shown to produce drops in comparable ranges, and refines the constraints on the number of drops being produced, especially for film drops, as they might shift the range of sizes at which one mechanism dominates over the other. Finally, as discussed above, further theoretical work is necessary in order to predict and model the sub-micrometer aerosols resulting from film drops in the present framework.

The resulting sea spray source function is fully compatible with typical functions used in the literature and reviewed by Lewis & Schwartz (2004), Veron (2015), and de Leeuw et al. (2011), indicating the strong potential of this approach, which incorporates temperature conditions and

physical dependency on sea state. The drop production is higher during the storm intensification than during the set-down, for the same wind speed, which explains some of the natural variability reported in existing field measurements.

5.4. Surfactants and the Physicochemistry of the Interface

We have discussed jet and film drops produced by bursting and considered the role of viscosity, density, and surface tension in determining the film thickness and cavity collapse, which control film and jet drop properties. The ocean surface is partly covered by a biofilm, which can be modeled as surfactant (Wurl et al. 2011), and surface-active contaminations for which the static tension is still close to its clean (uncontaminated) value are known to modify the static and dynamic behaviors of bubbles, including their coalescence, lifetimes, and bursting (Langevin & Rio 2015, Poulain et al. 2018, Néel & Deike 2021, Shaw & Deike 2021).

Néel & Deike (2021) considered a nearly monodisperse assembly of millimetric air bubbles produced identically in the bulk for a wide range of surface contamination and showed two asymptotic regimes: For low contamination, bubbles are short lived and coalesce systematically, with bubbles aggregating up to a hundred times their initial volume, leading to broad size distributions that are distinct from those for monodisperse bubbles. At high contamination, bubbles have extended lifetimes and coalescence is prevented so that the surface bubble distribution tends toward the bulk bubble distribution. The ocean water condition is expected to be in an intermediate regime (Néel & Deike 2021). This implies that knowledge of the bulk bubble distribution might not be enough to predict the surface bubble distribution, introducing a bulk surface transfer function, which depends on the bubble lifetime and merging capability, which is itself a function of the water contamination, temperature, and humidity conditions. This transfer function, once developed, could be integrated to the framework presented above, with the ability to modify the size distribution of bubbles bursting at the surface $Q(R_b)$ and the associated bounds of drop size and production efficiency.

Multiple experiments have attempted to describe the role of the physicochemical parameters on the production of droplets and aerosols by bursting bubbles. There are large variations in protocols and results sometimes contradict each other (Modini et al. 2013, Prather et al. 2013, Quinn et al. 2015, Bertram et al. 2018, Frossard et al. 2019) on whether enrichment by biological activity, and the presence of surfactants, might increase or decrease the production of sea spray aerosols. The composition of the sea surface microlayer has been shown to play a major role in the later composition of the aerosols, together with the spray production mechanisms (Cochran et al. 2017, Wang et al. 2017, Bertram et al. 2018). Combining the fluid mechanics of the production of jet and film drops with the associated chemical composition of water droplets and final solid sea spray aerosols remains to be proposed.

SUMMARY POINTS

1. Canonical studies of breaking waves, bubble dynamics in turbulence, and bubble bursting provide detailed descriptions of the local air–sea mass exchange.

2. Using a statistical representation of breaking waves and the resulting entrained air bubbles leads to a multiscale formulation of air–sea fluxes controlled by breaking waves, naturally encompassing sea state effects.

3. This framework is applied to propose a generic sea state–dependent bubble-mediated gas transfer velocity (for various species), which collapse field data for CO_2 and DMS (dimethylsulfide) by accounting for wave effects.

4. This framework is also applied to propose a sea state–dependent sea spray generation function due to bubble bursting for film and jet drops. The resulting sea spray generation is fully compatible with existing formulations.

5. This framework provides a modeling path to account for sea state variability in air–sea mass exchange and can easily be implemented in spectral wave models.

FUTURE ISSUES

1. The similarity hypothesis of breaking dynamics, air entrainment, and bubble statistics should be tested in the field through detailed near-surface measurements of the two-phase turbulent processes.

2. Systematic field observations of the breaking statistics, gas transfer, and near-surface spray production are necessary to further validate the proposed models.

3. The role of surface collective bubble dynamics on jet and film drop production needs to be evaluated, together with the role of contamination and its influence on the efficiency of jet and film drop production and the range of sizes produced.

4. The links between the physical mechanisms of spray formation and the aerosol chemical composition, which are starting to be better understood, need to be further developed and integrated in the mechanistic sea spray aerosol generation function, together with a clearer understanding of the role of temperature on the various processes.

5. The importance of sea state–dependent parameterizations of gas exchange and sea spray production on large-scale oceanic, atmospheric, and climatic dynamics needs to be assessed using coupled modeling.

6. The representation of breaking waves and associated gas and spray fluxes at very high wind speeds (above 25 m/s), where the definition of individual events ceases to be valid, remains an open challenge.

DISCLOSURE STATEMENT

The authors are not aware of any biases that might be perceived as affecting the objectivity of this review.

ACKNOWLEDGMENTS

LITERATURE CITED

Aliseda A, Lasheras J. 2011. Preferential concentration and rise velocity reduction of bubbles immersed in a homogeneous and isotropic turbulent flow. *Phys. Fluids* 23(9):093301

Ardhuin F, Rogers E, Babanin AV, Filipot JF, Magne R, et al. 2010. Semiempirical dissipation source functions for ocean waves. Part I: definition, calibration, and validation. *J. Phys. Oceanogr.* 40(9):1917–41

Atamanchuk D, Koelling J, Send U, Wallace D. 2020. Rapid transfer of oxygen to the deep ocean mediated by bubbles. *Nat. Geosci.* 13(3):232–37

Banner M, Peirson WL. 2007. Wave breaking onset and strength for two-dimensional deep-water wave groups. *J. Fluid Mech.* 585(1):93–115

Banner M, Zappa C, Gemmrich J. 2014. A note on the Phillips spectral framework for ocean whitecaps. *J. Phys. Oceanogr.* 44(7):1727–34

Bell TG, Landwehr S, Miller SD, Bruyn WJ, Callaghan AH, et al. 2017. Estimation of bubble-mediated air–sea gas exchange from concurrent DMS and CO_2 transfer velocities at intermediate–high wind speeds. *Atmos. Chem. Phys.* 17(14):9019–33

Berny A, Deike L, Séon T, Popinet S. 2020. Role of all jet drops in mass transfer from bursting bubbles. *Phys. Rev. Fluids* 5(3):033605

Berny A, Seon T, Popinet S, Deike L. 2021. Statistics of jet drop production. *Geophys. Res. Lett.* 48:e2021GL092919

Bertram TH, Cochran RE, Grassian VH, Stone EA. 2018. Sea spray aerosol chemical composition: elemental and molecular mimics for laboratory studies of heterogeneous and multiphase reactions. *Chem. Soc. Rev.* 47(7):2374–400

Blanchard DC. 1963. The electrification of the atmosphere by particles from bubbles in the sea. *Progr. Oceanogr.* 1:73–202

Blanchard DC, Syzdek LD. 1988. Film drop production as a function of bubble size. *J. Geophys. Res. Oceans* 93(C4):3649–54

Blanco-Rodríguez FJ, Gordillo J. 2020. On the sea spray aerosol originated from bubble bursting jets. *J. Fluid Mech.* 886:R2

Blenkinsopp CE, Chaplin JR. 2010. Bubble size measurements in breaking waves using optical fiber phase detection probes. *IEEE J. Ocean. Eng.* 35(2):388–401

Bowyer PA. 2001. Video measurements of near-surface bubble spectra. *J. Geophys. Res. Oceans* 106(C7):14179–90

Brasz CF, Bartlett CT, Walls PLL, Flynn EG, Yu YE, Bird JC. 2018. Minimum size for the top jet drop from a bursting bubble. *Phys. Rev. Fluids* 3(7):074001

Brumer S, Zappa C, Blomquist B, Fairall C, Cifuentes-Lorenzen A, et al. 2017a. Wave-related Reynolds number parameterizations of CO_2 and DMS transfer velocities. *Geophys. Res. Lett.* 44(19):9865–75

Brumer SE, Zappa CJ, Brooks IM, Tamura H, Brown SM, et al. 2017b. Whitecap coverage dependence on wind and wave statistics as observed during SO GasEx and HiWinGS. *J. Phys. Oceanogr.* 47(9):2211–35

Callaghan AH, de Leeuw G, Cohen L, O'Dowd CD. 2008. Relationship of oceanic whitecap coverage to wind speed and wind history. *Geophys. Res. Lett.* 35(23):L23609

Callaghan AH, Deane GB, Stokes MDM. 2013. Two regimes of laboratory whitecap foam decay: bubble-plume controlled and surfactant stabilized. *J. Phys. Oceanogr.* 43(6):1114–26

Callaghan AH, Deane GB, Stokes MD. 2017. On the imprint of surfactant-driven stabilization of laboratory breaking wave foam with comparison to oceanic whitecaps. *J. Geophys. Res. Oceans* 122(8):6110–28

Cavaleri L, Fox-Kemper B, Hemer M. 2012. Wind waves in the coupled climate system. *Bull. Am. Meteorol. Soc.* 93(11):1651–61

Chan WHR, Johnson PL, Moin P, Urzay J. 2020. The turbulent bubble break-up cascade. Part 2. Numerical simulations of breaking waves. arXiv:2009.04804 [physics.flu-dyn]

Chen G, Kharif C, Zaleski S, Li J. 1999. Two dimensional Navier–Stokes simulation of breaking waves. *Phys. Fluids* 11:121–33

Cipriano RJ, Blanchard DC. 1981. Bubble and aerosol spectra produced by a laboratory breaking wave. *J. Geophys. Res. Oceans* 86(C9):8085–92

Cochran RE, Ryder OS, Grassian VH, Prather KA. 2017. Sea spray aerosol: the chemical link between the oceans, atmosphere, and climate. *Acc. Chem. Res.* 50(3):599–604

de Leeuw G, Andreas EL, Anguelova MD, Fairall CW, Lewis ER, et al. 2011. Production flux of sea spray aerosol. *Rev. Geophys.* 49(2):RG2001

De Vita F, Verzicco R, Iafrati A. 2018. Breaking of modulated wave groups: kinematics and energy dissipation processes. *J. Fluid Mech.* 855:267–98

Deane GB, Stokes MD. 2002. Scale dependence of bubble creation mechanisms in breaking waves. *Nature* 418(6900):839–44

Deike L, Ghabache E, Liger-Belair G, Das AK, Zaleski S, et al. 2018. The dynamics of jets produced by bursting bubbles. *Phys. Rev. Fluids* 3:013603

Deike L, Lenain L, Melville WK. 2017a. Air entrainment by breaking waves. *Geophys. Res. Lett.* 44(8):3779–87

Deike L, Melville WK. 2018. Gas transfer by breaking waves. *Geophys. Res. Lett.* 45(19):10482–92

Deike L, Melville WK, Popinet S. 2016. Air entrainment and bubble statistics in breaking waves. *J. Fluid Mech.* 801:91–129

Deike L, Pizzo N, Melville WK. 2017b. Lagrangian mass transport by surface breaking waves. *J. Fluid Mech.* 829:364–91

Deike L, Popinet S, Melville WK. 2015. Capillary effects on wave breaking. *J. Fluid Mech.* 769:541–69

Derakhti M, Kirby JT. 2016. Breaking-onset, energy and momentum flux in unsteady focused wave packets. *J. Fluid Mech.* 790:553–81

Derakhti M, Kirby JT, Banner ML, Grilli ST, Thomson J. 2020. A unified breaking onset criterion for surface gravity water waves in arbitrary depth. *J. Geophys. Res. Oceans* 125(7):e2019JC015886

Dommermuth DG, Yue DK, Lin W, Rapp R, Chan E, Melville WK. 1988. Deep-water plunging breakers: a comparison between potential theory and experiments. *J. Fluid Mech.* 189:423–42

Drazen DA, Melville WK, Lenain L. 2008. Inertial scaling of dissipation in unsteady breaking waves. *J. Fluid Mech.* 611(1):307–32

Duchemin L, Popinet S, Josserand C, Zaleski S. 2002. Jet formation in bubbles bursting at a free surface. *Phys. Fluids* 14(9):3000–8

Duncan JH. 1981. An experimental investigation of breaking waves produced by a towed hydrofoil. *Proc. R. Soc. Lond. A* 377(1770):331–48

Duncan JH. 2001. Spilling breakers. *Annu. Rev. Fluid Mech.* 33:519–47

Edson J, Fairall C, Bariteau L, Zappa CJ, Cifuentes-Lorenzen A, et al. 2011. Direct covariance measurement of CO_2 gas transfer velocity during the 2008 Southern Ocean Gas Exchange Experiment: wind speed dependency. *J. Geophys. Res. Oceans* 116:C00F10

Eggers J, Villermaux E. 2008. Physics of liquid jets. *Rep. Prog. Phys.* 71(3):036601

Emerson S, Bushinsky S. 2016. The role of bubbles during air-sea gas exchange. *J. Geophys. Res. Oceans* 121(6):4360–76

Emerson S, Yang B, White M, Cronin M. 2019. Air-sea gas transfer: determining bubble fluxes with in situ N_2 observations. *J. Geophys. Res. Oceans* 124(4):2716–27

Erinin MA, Wang SD, Liu R, Towle D, Liu X, Duncan JH. 2019. Spray generation by a plunging breaker. *Geophys. Res. Lett.* 46(14):8244–51

Esters L, Landwehr S, Sutherland G, Bell TG, Christensen KH, et al. 2017. Parameterizing air-sea gas transfer velocity with dissipation. *J. Geophys. Res. Oceans* 122(4):3041–56

Fairall C, Bradley EF, Hare J, Grachev A, Edson J. 2003. Bulk parameterization of air–sea fluxes: updates and verification for the COARE algorithm. *J. Climate* 16(4):571–91

Farsoiya PK, Popinet S, Deike L. 2021. Bubble-mediated transfer of dilute gas in turbulence. *J. Fluid Mech.* 920:A34

Fitzgerald JW. 1975. Approximation formulas for the equilibrium size of an aerosol particle as a function of its dry size and composition and the ambient relative humidity. *J. Appl. Meteorol. Climatol.* 14(6):1044–49

Friedlingstein P, O'Sullivan M, Jones MW, Andrew RM, Hauck J, et al. 2020. Global carbon budget 2020. *Earth Syst. Sci. Data* 12(4):3269–340

Frossard AA, Long MS, Keene WC, Duplessis P, Kinsey JD, et al. 2019. Marine aerosol production via detrainment of bubble plumes generated in natural seawater with a forced-air Venturi. *J. Geophys. Res. Atmos.* 124(20):10931–50

Gañán-Calvo AM. 2017. Revision of bubble bursting: universal scaling laws of top jet drop size and speed. *Phys. Rev. Lett.* 119(20):204502

Garbe CS, Rutgersson A, Boutin J, de Leeuw G, Delille B, et al. 2014. Transfer across the air-sea interface. In *Ocean-Atmosphere Interactions of Gases and Particles*, ed. PS Liss, MT Johnson, pp. 55–112. Berlin: Springer-Verlag

Garrett C, Li M, Farmer D. 2000. The connection between bubble size spectra and energy dissipation rates in the upper ocean. *J. Phys. Oceanogr.* 30(9):2163–71

Gemmrich JR, Banner ML, Garrett C. 2008. Spectrally resolved energy dissipation rate and momentum flux of breaking waves. *J. Phys. Oceanogr.* 38(6):1296–312

Ghabache E. 2015. *Surface libre hors équilibre: de l'effondrement de cavité aux jets étirés* [Free surface out of equilibrium: from cavity collapse to stretched jets]. PhD Thesis, Univ. Pierre Marie Curie, Paris (In French)

Ghabache E, Antkowiak A, Josserand C, Séon T. 2014. On the physics of fizziness: how bubble bursting controls droplets ejection. *Phys. Fluids* 26:121701

Ghabache E, Séon T. 2016. Size of the top jet drop produced by bubble bursting. *Phys. Rev. Fluids* 1:051901(R)

Gordillo J, Rodríguez-Rodríguez J. 2019. Capillary waves control the ejection of bubble bursting jets. *J. Fluid Mech.* 867:556–71

Grare L, Peirson WL, Branger H, Walker JW, Giovanangeli JP, Makin V. 2013. Growth and dissipation of wind-forced, deep-water waves. *J. Fluid Mech.* 722:5–50

Hasselmann K. 1962. On the non-linear energy transfer in a gravity-wave spectrum. *J. Fluid Mech.* 12(15):481–500

Hasselmann K, Barnett TP, Bouws E, Carlson H, Cartwright DE, et al. 1973. *Measurements of wind-wave growth and swell decay during the Joint North Sea Wave Project (JONSWAP)*. Eng. Rep., Ergänzungsh. 8-12, Dtsch. Hydrogr. Inst., Hambg., Ger.

Hinze JO. 1955. Fundamentals of the hydrodynamic mechanism of splitting in dispersion processes. *AIChE J.* 1(3):289–95

Ho DT, Law CS, Smith MJ, Schlosser P, Harvey M, Hill P. 2006. Measurements of air-sea gas exchange at high wind speeds in the Southern Ocean: implications for global parameterizations. *Geophys. Res. Lett.* 33(16):L16611

Ho DT, Wanninkhof R, Schlosser P, Ullman DS, Hebert D, Sullivan KF. 2011. Toward a universal relationship between wind speed and gas exchange: gas transfer velocities measured with ^{3}He/SF$_6$ during the Southern Ocean Gas Exchange Experiment. *J. Geophys. Res. Oceans* 116:C00F04

Iafrati A. 2009. Numerical study of the effects of the breaking intensity on wave breaking flows. *J. Fluid Mech.* 622:371–411

Keeling RF. 1993. On the role of large bubbles in air-sea gas exchange and supersaturation in the ocean. *J. Mar. Res.* 51(2):237–71

Kleiss JM, Melville WK. 2010. Observations of wave breaking kinematics in fetch-limited seas. *J. Phys. Oceanogr.* 40(12):2575–604

Komen GJ, Cavaleri L, Donelan M, Hasselmann K, Hasselmann S, Janssen P. 1996. *Dynamics and Modelling of Ocean Waves*. Cambridge, UK: Cambridge Univ. Press

Lai CY, Eggers J, Deike L. 2018. Bubble bursting: universal cavity and jet profiles. *Phys. Rev. Lett.* 121(14):144501

Lamarre E, Melville W. 1991. Air entrainment and dissipation in breaking waves. *Nature* 351:469–72

Langevin D, Rio E. 2015. Foams and emulsions: coalescence. In *Encyclopedia of Surface and Colloid Science*, ed. P Somasundaran, N Deo, R Farinato, V Grassian, M Lu, et al., pp. 2837–51. Boca Raton, FL: CRC. 3rd ed.

Leighton TG, Coles DG, Srokosz M, White PR, Woolf DK. 2018. Asymmetric transfer of CO$_2$ across a broken sea surface. *Sci. Rep.* 8:8301

Lenain L, Melville WK. 2017a. Evidence of sea-state dependence of aerosol concentration in the marine atmospheric boundary layer. *J. Phys. Oceanogr.* 47:69–84

Lenain L, Melville WK. 2017b. Measurements of the directional spectrum across the equilibrium saturation ranges of wind-generated surface waves. *J. Phys. Oceanogr.* 47(8):2123–38

Lenain L, Pizzo N. 2020. The contribution of high-frequency wind-generated surface waves to the Stokes drift. *J. Phys. Oceanogr.* 50(12):3455–65

Levich VG. 1962. *Physicochemical Hydrodynamics.* Englewood Cliffs, NJ: Prentice-Hall

Lewis ER, Schwartz SE. 2004. *Sea Salt Aerosol Production: Mechanisms, Methods, Measurements, and Models.* Washington, DC: Am. Geophys. Union

Lhuissier H, Villermaux E. 2012. Bursting bubble aerosols. *J. Fluid Mech.* 696:5–44

Liang J-H, Emerson SR, D'Asaro EA, McNeil CL, Harcourt RR, et al. 2017. On the role of sea-state in bubble-mediated air-sea gas flux during a winter storm. *J. Geophys. Res. Oceans* 122(4):2671–85

Liang J-H, McWilliams JC, Sullivan PP, Baschek B. 2011. Modeling bubbles and dissolved gases in the ocean. *J. Geophys. Res.* 116:C03015

Liang J-H, McWilliams JC, Sullivan PP, Baschek B. 2012. Large eddy simulation of the bubbly ocean: new insights on subsurface bubble distribution and bubble-mediated gas transfer. *J. Geophys. Res.* 117:C04002

Liss PS, Merlivat L. 1986. Air-sea gas exchange rates: introduction and synthesis. In *The Role of Air-Sea Exchange in Geochemical Cycling*, ed. P Buat-Ménard, pp. 113–27. Dordrecht, Neth.: Springer

Loewen MR, O'Dor MA, Skafel MG. 1996. Bubbles entrained by mechanically generated breaking waves. *J. Geophys. Res.* 101(C9):20759–69

Longuet-Higgins MS. 1957. The statistical analysis of a random, moving surface. *Philos. Trans. R. Soc. A* 249(966):321–87

Longuet-Higgins MS, Dommermuth DG. 1997. Crest instabilities of gravity waves. Part 3. Nonlinear development and breaking. *J. Fluid Mech.* 336:33–50

Lubin P, Glockner S. 2015. Numerical simulations of three-dimensional plunging breaking waves: generation and evolution of aerated vortex filaments. *J. Fluid Mech.* 767:364–93

Mårtensson E, Nilsson E, de Leeuw G, Cohen L, Hansson HC. 2003. Laboratory simulations and parameterization of the primary marine aerosol production. *J. Geophys. Res. Atmos.* 108(D9):4297

Martinez-Bazan C, Montanes J, Lasheras J. 1999. On the breakup of an air bubble injected into a fully developed turbulent flow. Part 1. Breakup frequency. *J. Fluid Mech.* 401:157–82

Melville WK. 1982. The instability and breaking of deep-water waves. *J. Fluid Mech.* 115:165–85

Melville WK. 1994. Energy dissipation by breaking waves. *J. Phys. Oceanogr.* 24:2041–49

Melville WK. 1996. The role of surface-wave breaking in air-sea interaction. *Annu. Rev. Fluid Mech.* 28:279–321

Melville WK, Fedorov AV. 2015. The equilibrium dynamics and statistics of gravity–capillary waves. *J. Fluid Mech.* 767:449–66

Melville WK, Veron F, White CJ. 2002. The velocity field under breaking waves: coherent structure and turbulence. *J. Fluid Mech.* 454:203–33

Miles JW. 1957. On the generation of surface waves by shear flows. *J. Fluid Mech.* 3(2):185–204

Miller S, Marandino C, De Bruyn W, Saltzman E. 2009. Air-sea gas exchange of CO_2 and DMS in the North Atlantic by eddy covariance. *Geophys. Res. Lett.* 36:L15816

Modini R, Russell L, Deane G, Stokes M. 2013. Effect of soluble surfactant on bubble persistence and bubble-produced aerosol particles. *J. Geophys. Res. Atmos.* 118(3):1388–400

Monahan EC, Muircheartaigh I. 1980. Optimal power-law description of oceanic whitecap coverage dependence on wind speed. *J. Phys. Oceanogr.* 10(12):2094–99

Mostert W, Popinet S, Deike L. 2021. High-resolution direct simulation of deep water breaking waves: transition to turbulence, bubbles and droplets production. arXiv:2103.05851 [physics.flu-dyn]

Mueller J, Veron F. 2009. A sea state-dependent spume generation function. *J. Phys. Oceanogr.* 39(9):2363–72

Néel B, Deike L. 2021. Collective bursting of free-surface bubbles, and the role of surface contamination. *J. Fluid Mech.* 917:A46

Néel B, Villermaux E. 2018. The spontaneous puncture of thick liquid films. *J. Fluid Mech.* 838:192–21

Nightingale PD, Malin G, Law CS, Watson AJ, Liss PS, et al. 2000. In situ evaluation of air-sea gas exchange parameterization using novel conservative and volatile tracers. *Glob. Biogeochem. Cycles* 14:373–87

Ortiz-Suslow DG, Haus BK, Mehta S, Laxague NJ. 2016. Sea spray generation in very high winds. *J. Atmos. Sci.* 73(10):3975–95

Perlin M, Choi W, Tian Z. 2013. Breaking waves in deep and intermediate waters. *Annu. Rev. Fluid Mech.* 45:115–45

Perrard S, Rivière A, Mostert W, Deike L. 2021. Bubble deformation by a turbulent flow. *J. Fluid Mech.* 920:A15

Phillips O. 1985. Spectral and statistical properties of the equilibrium range in wind-generated gravity waves. *J. Fluid Mech.* 156:505–31

Pizzo N, Deike L, Melville WK. 2016. Current generation by deep-water breaking waves. *J. Fluid Mech.* 803:275–91

Pizzo N, Melville WK. 2013. Vortex generation by deep-water breaking waves. *J. Fluid Mech.* 734:198–218

Pizzo N, Melville WK, Deike L. 2019. Lagrangian transport by nonbreaking and breaking deep-water waves at the ocean surface. *J. Phys. Oceanogr.* 49(4):983–92

Plant WJ. 1982. A relationship between wind stress and wave slope. *J. Geophys. Res. Oceans* 87(C3):1961–67

Poorte RE, Biesheuvel A. 2002. Experiments on the motion of gas bubbles in turbulence generated by an active grid. *J. Fluid Mech.* 461:127–54

Poulain S, Villermaux E, Bourouiba L. 2018. Ageing and burst of surface bubbles. *J. Fluid Mech.* 851:636–71

Prather KA, Bertram TH, Grassian VH, Deane GB, Stokes MD, et al. 2013. Bringing the ocean into the laboratory to probe the chemical complexity of sea spray aerosol. *PNAS* 110(19):7550–55

Quinn PK, Collins DB, Grassian VH, Prather KA, Bates TS. 2015. Chemistry and related properties of freshly emitted sea spray aerosol. *Chem. Rev.* 115(10):4383–99

Rapp R, Melville W. 1990. Laboratory measurements of deep-water breaking waves. *Philos. Trans. R. Soc. A* 331:735–800

Reichl BG, Deike L. 2020. Contribution of sea-state dependent bubbles to air-sea carbon dioxide fluxes. *Geophys. Res. Lett.* 47(9):e2020GL087267

Resch F, Afeti G. 1991. Film drop distributions from bubbles bursting in seawater. *J. Geophys. Res. Oceans* 96(C6):10681–88

Richter DH, Dempsey AE, Sullivan PP. 2019. Turbulent transport of spray droplets in the vicinity of moving surface waves. *J. Phys. Oceanogr.* 49(7):1789–807

Rivière A, Mostert W, Perrard S, Deike L. 2021. Sub-Hinze scale bubble production in turbulent bubble break-up. *J. Fluid Mech.* 917:A40

Rojas G, Loewen M. 2007. Fiber-optic probe measurements of void fraction and bubble size distributions beneath breaking waves. *Exp. Fluids* 43(6):895–906

Romero L. 2019. Distribution of surface wave breaking fronts. *Geophys. Res. Lett.* 46(17–18):10463–74

Romero L, Melville WK. 2010. Airborne observations of fetch-limited waves in the Gulf of Tehuantepec. *J. Phys. Oceanogr.* 40(3):441–65

Romero L, Melville WK. 2011. Spatial statistics of the sea surface in fetch-limited conditions. *J. Phys. Oceanogr.* 41(10):1821–41

Romero L, Melville WK, Kleiss JM. 2012. Spectral energy dissipation due to surface wave breaking. *J. Phys. Oceanogr.* 42:1421–41

Ruth DJ, Vernet M, Perrard S, Deike L. 2021. The effect of nonlinear drag on the rise velocity of bubbles in turbulence. *J. Fluid Mech.* 924:A2

Saket A, Peirson WL, Banner ML, Barthelemy X, Allis MJ. 2017. On the threshold for wave breaking of two-dimensional deep water wave groups in the absence and presence of wind. *J. Fluid Mech.* 811:642–58

Salibindla AK, Masuk AUM, Tan S, Ni R. 2020. Lift and drag coefficients of deformable bubbles in intense turbulence determined from bubble rise velocity. *J. Fluid Mech.* 894:A20

Schwendeman M, Thomson J. 2015. Observations of whitecap coverage and the relation to wind stress, wave slope, and turbulent dissipation. *J. Geophys. Res. Oceans* 120(12):8346–63

Schwendeman M, Thomson J, Gemmrich JR. 2014. Wave breaking dissipation in a young wind sea. *J. Phys. Oceanogr.* 44(1):104–27

Sellegri K, O'Dowd C, Yoon Y, Jennings S, de Leeuw G. 2006. Surfactants and submicron sea spray generation. *J. Geophys. Res. Atmos.* 111:D22215

Shaw D, Deike L. 2021. Surface bubble coalescence. *J. Fluid Mech.* 915:A105

Soligo G, Roccon A, Soldati A. 2019. Breakage, coalescence and size distribution of surfactant-laden droplets in turbulent flow. *J. Fluid Mech.* 881:244–82

Spiel DE. 1994. The number and size of jet drops produced by air bubbles bursting on a fresh water surface. *J. Geophys. Res.* 99(C5):10289–96

Spiel DE. 1997. More on the births of jet drops from bubbles bursting on seawater surfaces. *J. Geophys. Res.* 102(C3):5815–21

Stanley RH, Jenkins WJ, Lott DE 3rd, Doney SC. 2009. Noble gas constraints on air-sea gas exchange and bubble fluxes. *J. Geophys. Res. Oceans* 114:C11020

Sullivan PP, McWilliams JC. 2010. Dynamics of winds and currents coupled to surface waves. *Annu. Rev. Fluid Mech.* 42:19–42

Sutherland P, Melville WK. 2013. Field measurements and scaling of ocean surface wave-breaking statistics. *Geophys. Res. Lett.* 40(12):3074–79

Sutherland P, Melville WK. 2015. Field measurements of surface and near-surface turbulence in the presence of breaking waves. *J. Phys. Oceanogr.* 45(4):943–65

Thomson J, Gemmrich JR, Jessup AT. 2009. Energy dissipation and the spectral distribution of whitecaps. *Geophys. Res. Lett.* 36:L11601

Tian Z, Perlin M, Choi W. 2010. Energy dissipation in two-dimensional unsteady plunging breakers and an eddy viscosity model. *J. Fluid Mech.* 655:217–57

Toba Y. 1972. Local balance in the air-sea boundary processes. *J. Oceanogr.* 28(3):109–20

Troitskaya Y, Kandaurov A, Ermakova O, Kozlov D, Sergeev D, Zilitinkevich S. 2018. The "bag breakup" spume droplet generation mechanism at high winds. Part I: spray generation function. *J. Phys. Oceanogr.* 48(9):2167–88

Tsai WT, Hung L. 2007. Three-dimensionnal modeling of small-scale processes in the upper boundary layer bounded by a dynamic ocean surface. *J. Geophys. Res.* 112:C02019

Veron F. 2015. Ocean spray. *Annu. Rev. Fluid Mech.* 47:507–38

Veron F, Hopkins C, Harrison E, Mueller J. 2012. Sea spray spume droplet production in high wind speeds. *Geophys. Res. Lett.* 39:L16602

Villermaux E. 2020. Fragmentation versus cohesion. *J. Fluid Mech.* 898:P1

Walls P, Henaux L, Bird JC. 2015. Jet drops from bursting bubbles: how gravity and viscosity couple to inhibit droplet production. *Phys. Rev. E* 92(2):021002

Wang X, Deane GB, Moore KA, Ryder OS, Stokes MD, et al. 2017. The role of jet and film drops in controlling the mixing state of submicron sea spray aerosol particles. *PNAS* 114(27):6978–83

Wang Z, Yang J, Stern F. 2016. High-fidelity simulations of bubble, droplet and spray formation in breaking waves. *J. Fluid Mech.* 792:307–27

Wanninkhof R. 1992. Relationship between wind speed and gas exchange over the ocean. *J. Geophys. Res. Oceans* 97:7373–82

Wanninkhof R. 2014. Relationship between wind speed and gas exchange over the ocean revisited. *Limnol. Oceanogr. Methods* 12(6):351–62

Wanninkhof R, Asher W, Ho D, Sweeney C, McGillis W. 2009. Advances in quantifying air-sea gas exchange and environmental forcing. *Annu. Rev. Mar. Sci.* 1:213–44

Wanninkhof R, McGillis WR. 1999. A cubic relationship between air-sea CO_2 exchange and wind speed. *Geophys. Res. Lett.* 26:1889–92

Woolf DK. 2005. Parametrization of gas transfer velocities and sea-state-dependent wave breaking. *Tellus B* 57(2):87–94

Woolf DK, Bowyer PA, Monahan EC. 1987. Discriminating between the film drops and jet drops produced by a simulated whitecap. *J. Geophys. Res. Oceans* 92(C5):5142–50

Woolf DK, Shutler JD, Goddijn-Murphy L, Watson A, Chapron B, et al. 2019. Key uncertainties in the recent air-sea flux of CO_2. *Glob. Biogeochem. Cycles* 33(12):1548–63

Woolf DK, Thorpe S. 1991. Bubbles and the air-sea exchange of gases in near-saturation conditions. *J. Mar. Res.* 49(3):435–66

Wurl O, Wurl E, Miller L, Johnson K, Vagle S. 2011. Formation and global distribution of sea-surface microlayers. *Biogeosciences* 8(1):121–35

Yang Z, Deng BQ, Shen L. 2018. Direct numerical simulation of wind turbulence over breaking waves. *J. Fluid Mech.* 850:120–55

Zakharov VE, Badulin SI, Hwang PA, Caulliez G. 2015. Universality of sea wave growth and its physical roots. *J. Fluid Mech.* 780:503–35

Zakharov VE, L'vov VS, Falkovich G. 2012. *Kolmogorov Spectra of Turbulence I: Wave Turbulence*. Berlin: Springer-Verlag

Zappa CJ, Asher WE, Jessup AT. 2001. Microscale wave breaking and air-water gas transfer. *J. Geophys. Res. Oceans* 106(C5):9385–91

Zappa CJ, Banner M, Schultz H, Gemmrich J, Morison R, et al. 2012. An overview of sea state conditions and air-sea fluxes during RaDyO. *J. Geophys. Res. Oceans* 117:C00H19

Contents

Indexes

Errata

An online log of corrections to *Annual Review of Fluid Mechanics* articles may be found
at http://www.annualreviews.org/errata/fluid